

## Optical Rotation Curves and Linewidths for Tully-Fisher Applications <sup>1</sup>

Stéphane Courteau

Kitt Peak National Observatory, 950 North Cherry Avenue, Tucson, AZ 85726 <sup>2</sup>

### ABSTRACT

We present optical long-slit rotation curves (RCs) for 304 northern Sb-Sc UGC galaxies originally selected for Tully-Fisher (TF) applications. Matching  $r$ -band photometry exists for each galaxy. We describe the procedures of RC extraction and construction of optical profiles analogous to 21cm integrated linewidths. More than 20% of the galaxies were observed twice or more, allowing for a proper determination of systematic errors. Various measures of maximum rotational velocity to be used as input in the TF relation are tested on the basis of their repeatability, minimization of TF scatter, and match with 21cm linewidths. The best measure of TF velocity,  $V_{2.2}$ , is given at the location of peak rotational velocity of a pure exponential disk. An alternative measure to  $V_{2.2}$  which makes no assumption about the luminosity profile or shape of the rotation curve is  $V_{hist}$ , the 20% width of the velocity histogram, though the match with 21cm linewidths is not as good. We show that optical TF calibrations yield internal scatter comparable to, if not smaller than, the best calibrations based on single-dish 21cm radio linewidths. Even though resolved H I RCs are more extended than their optical counterpart, a tight match between optical and radio linewidths exists since the bulk of the H I surface density is enclosed within the optical radius.

We model the 304 RCs presented here and a sample of 958 curves from Mathewson *et al.* (1992) with various fitting functions. An arctan function provides an adequate simple fit (not accounting for non-circular motions and spiral arms). More elaborate, empirical models may yield a better match at the expense of strong covariances. We caution against physical or “universal” parameterizations for TF applications.

*Subject headings:* galaxies: spectroscopy — galaxies: spiral - surveys

---

<sup>1</sup>Based on observations made at Lick (UCO) and Las Campanas (OCIW) Observatories.

<sup>2</sup>Current Address: Herzberg Institute for Astrophysics, Dominion Astrophysical Observatory, 5071 W. Saanich Rd., Victoria, B.C. V8X 4M6. email: stephane.courteau@hia.nrc.ca

## 1. Introduction

Since the pioneering work of Oepik (1922), it has been understood that rotational velocities and apparent magnitudes could be used to infer extragalactic distances (cf. *e.g.* Rubin 1995). Work on correlations between rotational velocities and diameter or luminosity in the 1960s and early 1970s (Roberts 1969, Bottinelli *et al.* 1971, Balkowski *et al.* 1974, Shostak 1975, Roberts 1975, Sandage & Tammann 1976) led to the definitive formulation of the Tully-Fisher relation (Tully & Fisher 1977; hereafter TF) which has become one of the most powerful and widely used tools for studying cosmic velocity fields in the local universe (cf. Strauss & Willick 1995 for a review).

The TF relation is an empirical correlation between some suitably defined measure of the “peak” circular velocity (or linewidth),  $V$ , and the total absolute magnitude,  $M$ , of a spiral galaxy, such that  $M = a \log V + b$ . Together, these two parameters define a plane of structural parameters for spiral galaxies which may reflect the way they were initially formed or perhaps suggest the presence of self-regulating processes of star formation in galactic disks. There are several models of galaxy formation which predict of a correlation between the luminosity and rotation velocity for spiral galaxies (Fall & Efstathiou 1980, Faber 1982, Gunn 1982, Blumenthal *et al.* 1984, Ashman 1990, Cole *et al.* 1994, Eisenstein & Loeb 1995, Eisenstein 1996). A correlation is expected, as both luminosity and disk rotational velocity depend on galaxy mass. An alternative model for the TF relation involves dissipative galaxy formation in which regulated star formation, or the ability of the galaxy to retain gas ejected from stars and supernovae, is determined by the amount of baryonic matter in the halo. In this model, the TF relation arises as a natural “prediction” with negligible scatter (White 1991, Kauffmann *et al.* 1993, Silk 1995, 1997). The residuals in the TF relation must therefore reflect fluctuations in the detailed formation and enrichment history of galactic halos. Evolution and environmental effects are therefore likely to modify the shape of the TF relation in different environments and would suggest that a true universal TF relation  $L \propto V^3$  does not exist.

Various TF calibrations will be obtained depending upon the choice of photometric bandpass and measure of rotational speed. These, in addition to corrections for various intrinsic, environmental, and instrumental biases, all contribute to the shape, zero-point, and scatter of the TF relation. It is now well understood that the slope and zero-point of the TF relation depend strongly on aperture and bandpass and that a smaller dispersion is obtained for near-IR (NIR) bandpasses ( $R$ ,  $I$ , and  $H$ ) than for the  $B$  or  $V$  bands. As first argued by Aaronson and coworkers in the 80’s (*e.g.* Aaronson *et al.* 1989 and references therein), infrared photometry suffers less from Galactic and internal absorption corrections than do bluer bandpasses. Moreover, it is mostly sensitive to the underlying evolved stellar population which best traces the optical mass and thus correlates more tightly with the maximum rotational speed or, total galaxy mass. Inclinations are also better determined at infrared wavebands since the overall image is smoother (Peletier & Willner 1993).

There is a well-known trend of increasing TF slopes toward longer wavelengths; representative ranges for the  $B$ ,  $R$ ,  $I$ , and  $H$  bandpasses are roughly 5, 6, 7 and  $8^3$  respectively (Strauss & Willick 1995, Willick *et al.* 1997, hereafter W97). The typical slope for a linear TF relation is close to 7.5 for the red and infrared bands indicating that  $L_{R/IR} \propto V_{\max}^3$ . The typical intrinsic rms dispersion of the best forward<sup>4</sup> TF calibrations, with carefully measured CCD magnitudes and inclinations, is between 0.25-0.40 mag ( $1\sigma$ ) or a 12-20% distance error. TF scatters as low as 0.1 mag have been reported for pruned samples with very specific selection criteria (Bothun & Mould 1987, Pierce & Tully 1992, Rood & Williams 1993, Bernstein *et al.* 1994, Raychaudhury *et al.* 1997, hereafter R97) but these do not reflect the normal population sampled in larger TF surveys. Recent NIR TF investigations in  $r$  and  $I$  bandpasses have yielded comparable, if not smaller, TF dispersions than similar  $H$ -band TF calibrations (Pierce & Tully 1992, Willick 1991, Han 1991, Courteau 1992 (hereafter C92), Mathewson *et al.* 1992 (hereafter MAT), Peletier & Willner 1993, Schommer *et al.* 1993, Bernstein *et al.* 1994, W97, Giovanelli *et al.* 1997 (hereafter G97), R97). No advantage is gained by imaging at yet longer wavelengths. As underscored by Rhee (1996), the  $K$ -band TF scatter is significantly larger on account of a less stable sky background and greater sensitivity to stellar population effects (cf. Regan & Vogel 1994, Rhoads 1997). The latter will induce greater uncertainty in inclination estimates as well. TF scatter increases significantly at longer wavelengths where emission is mostly dominated by dust. In fact, the TF relation disappears beyond  $10\mu\text{m}$ , though the greater scatter reported in the  $L$ -band is also largely due to higher instrumental noise and smaller galaxy fluxes (Malhotra *et al.* 1997).

While photometric bandpass is an important contributor to the TF slope and zero-point, the specific definition of linewidths is equally fundamental. For example, the TF calibrations for MAT and Han-Mould galaxies are both based on I-band imaging yet they differ in slope by as much as a unit due to different linewidth definitions (W97). The former study uses resolved optical RCs (ORCs) and the latter is based on integrated radio linewidths. There is thus strong impetus to understand systematic effects due to the choice of linewidths. Besides *intrinsic* or *cosmic* scatter, raw linewidths *per se* are the leading source of dispersion in the overall TF error budget (Schommer *et al.* 1993, C92). Photometric inclination errors are a close second (Pierce & Tully 1988, Peletier & Willner 1991, Willick 1991, C92). The magnitude dispersion induced by inclination scatter (for a given internal extinction correction) is only  $\sim 0.04$ - $0.05$  mag, and the total error on fully processed magnitudes is typically 0.06-0.08 mag (Schommer *et al.* 1993, Courteau 1996). Linewidths are more severely impacted. Inclination errors account for about 0.10 mag of the total linewidth error which is typically 0.20 mag (C92, G97). This is greater

---

<sup>3</sup> Note that this infrared TF slope (Bernstein *et al.* 1994) is appreciably closer to optical slopes than the canonical Aaronson value of  $\sim 10$ . The larger slope observed at  $H$ -band by Aaronson *et al.* (1982) was shown to be largely due to aperture effects (Willick 1991). Pierce & Tully (1992) also obtain a steep slope at  $H$  which is mostly due to their “inverse” fitting approach.

<sup>4</sup>cf. Strauss & Willick (1995) or Willick *et al.* (1996) for a discussion of forward vs inverse fitting techniques and inherent biases. In this paper, we concern ourselves only with the forward approach.

than the dispersion of  $\sim 0.15$  induced by axisymmetric deviations in galactic disks (Franx & de Zeeuw 1992, Rix & Zaritzky 1995). Other sources collectively labelled as “cosmic scatter” may contribute a substantial share of the TF error budget but none independently as large as that from raw linewidth measurements (W97 show that the overall cosmic scatter is  $\sim 0.30$  mag). One must therefore proceed with Procrustean care when defining a TF linewidth.

It has also been demonstrated that the TF residuals are mostly Gaussian (W97) and not a function of any likely “third parameter” such as central and mean surface brightnesses, bulge-to-disk ratios, RC shape, concentration indices, morphological type, colors, etc. (Schlegel 1995, Courteau & Rix 1997 (CR97), W97; see however G97, Giraud 1986, Bothun & Mould 1987). Spiral galaxies, in this sense, truly define a one-parameter sequence. After correction for various observational effects, the TF dispersion appears to have been reduced to its minimum dispersion in the luminosity-linewidth plane of spiral galaxies.

Measurements of TF rotational velocities have primarily relied on single-dish radio observations of neutral hydrogen at 21cm. However, the restricted sky coverage of the Arecibo and Nançay radio-telescopes, lack of correlator power of array instruments, and lower sensitivity of steerable dishes constitute crucial limitations for any H I -based TF survey. Emission lines traced in the optical domain provide a most adequate substitute to 21cm emission. The good match between radio and optical velocity widths has been emphasized by Thonnard (1983) and further verified by Courteau & Faber (1988), C92, MAT, and Vogt (1994). Considerable effort has been invested in recent years in large TF surveys based on ORCs or integrated optical profiles (Dressler & Faber 1990, C92, MAT, Schommer *et al.* 1993, Vogt 1994, Schlegel 1995, G97.) The goal of this paper is to address technical issues which pertain to the extraction and analysis of long-slit optical spectra for TF applications.

We present below a detailed account of the acquisition and calibration of long-slit ORCs for TF applications. We use a sample of 304 UGC field Sb-Sc spirals with H $\alpha$  spectra and  $r$ -band photometry drawn from the collection of field Sb-Sc spirals of Courteau (1992; hereafter C92). This sample is also referred to as “Courteau-Faber” (hereafter CF). Multiple observations for 62 galaxies combine for a total of 132 spectra which will be used to study systematics and errors.

Sample selection, catalog information, redshift histograms, sky distribution, and photometric reductions were all presented in Courteau (1996; hereafter Paper I). The division of this paper is as follow: In §2 we discuss the spectroscopic observations and data reduction. The extraction of rotation curves from resolved emission lines is discussed in §3 and in §4, we compare our results with the long-slit RCs of Rubin and coworkers, Vogt (1994), and the Fabry-Perot RCs of Amram *et al.* (1992, 1994). The reader familiar with RC extractions can skip to §5 without loss of continuity. We address various issues of RC shapes and fitting models in §5, which includes a brief discussion of the applicability of the “Universal Rotation Curve” of Persic, Salucci, & Stel (1996; hereafter PSS). We introduce various definitions of velocity measurements for TF use both from resolved RCs and integrated profiles in §6. In §7, we make use of repeat observations to investigate the

internal stability of our data. Corrections to resolved and integrated linewidths are shown in §8, and we assemble a table of corrected data in §9. Optical TF calibrations are derived in §10 and we examine the tight match between optical and radio linewidths in §11. Three appendices include A) a presentation of all the CF RCs, two-sided and folded, and best-fitting models; B) model parameters for all fitted CF ORCs and the 958 ORCs from the compilation of MAT; and C) a discussion on intensity-weighted centroids and the use of parabolic interpolation for binned data.

Throughout the paper, we make the distinction between three measures of rotational linewidths. We shall refer to the velocity separation between the approaching and receding sides of the resolved RC as  $\Delta V$  (*e.g.*  $\Delta V_{max}$ ). The width of any one-dimensional (integrated) rotation profile, be it a fully convolved 21cm spectrum or a co-added or unresolved optical spectrum, will be called  $W$  (*e.g.*  $W_{20}, W_{50}$ ). A velocity measured from a one-sided resolved rotation curve will simply be denoted as  $V$  (*e.g.*  $V_{2.2}, V_{iso}, V_{max}, V_{opt}$ ). Physical scales are calculated using  $H_0 = 70 \text{ km s}^{-1} \text{ Mpc}^{-1}$ .

## 2. Spectroscopic Observations and Data Reduction

Spectroscopic observations were made at Lick Observatory using the UV Schmidt Cassegrain Spectrograph on the Shane 3.0m telescope (Miller & Stone 1987) and at Las Campanas with the Modular Spectrograph on the 2.5m du Pont telescope. Table 1 summarizes the main characteristics of both instrumental setups. A total of 453  $H\alpha$  spectra, including repeats, was collected at Lick (43 nights) and Las Campanas (1 night courtesy of Alan Dressler). Only ten spectra showed no measurable signal. The final collection of RCs includes measurements for 304 galaxies, 62 of them were observed more than once. Eight galaxies were observed twice as a consistency check between Lick and Las Campanas. Minor axis RCs for 6 galaxies were also observed to verify the lack of significant velocity gradients.

The nominal exposure times (Table 1) were chosen to sample at least the maxima of the rotation curve on both the approaching and receding sides, but do not allow for measurements at very faint light levels. Typically, the rotation curve ends just beyond the optical radius (defined here as 3.2 disk scale lengths - see Fig. 4). Most galaxies were fully sampled within the 2' slit.

As in Paper I, the bulk of our reductions was based on the interactive image-reduction package VISTA<sup>5</sup> originally developed at Lick Observatory (Lauer, Stover, & Terndrup 1983). The reduction procedures described below are available from the author as VISTA routines.

Red spectra of spiral galaxies at low redshifts typically show the prominent nebular lines of  $H\alpha$   $\lambda 6563$ , [N II]  $\lambda\lambda 6548, 6583$ , and [S II]  $\lambda\lambda 6716, 6731$  with a relative range of intensities. While nuclear [N II] may sometimes exceed  $H\alpha$  in strength the disk emission is usually stronger at  $H\alpha$

---

<sup>5</sup>VISTA is currently maintained by Jon Holtzman at New Mexico State University. The official release is available via anonymous FTP to vista@nmsu.edu.

TABLE 1  
CCD/Telescope Parameters

	Lick	Las Campanas
Telescope	Shane 3.0m	du Pont 2.5m
Spectrograph	UV Schmidt	Modular
Grating	1200 $\ell$ /mm	1200 $\ell$ /mm
Blaze (1 <sup>st</sup> order)	5000 Å	7500 Å
Camera (Nikkor)	58mm f/1.2	85mm f/1.4
Spectral coverage	6150–6950 Å	6080–7290 Å
Slit width	2''8 × 2'	2''5 × 2'
Spatial scale	0''66/15 $\mu$ -pixel	0''85/15 $\mu$ -pixel
Dispersion (at H $\alpha$ )	1.019 Å/15 $\mu$ -pixel	1.515 Å/15 $\mu$ -pixel
Reduced log dispersion	48.5 km s <sup>-1</sup> /bin	75 km s <sup>-1</sup> /bin
Resolution (FWHM)	~ 2.7 Å	~ 4.5 Å
Detector	TI 3-phase 800×800 CCD	
Readout noise	7e <sup>-</sup>	13e <sup>-</sup>
Gain (ADU)	2.6e <sup>-</sup> /DN	1.5e <sup>-</sup> /DN
Exposure time	1800 s	1500 s
Net Instrument Eff. <sup>a</sup>	~ 15%	not measured

a) Net Instrumental Efficiency (telescope, spectrograph, detector) measured at ~ H $\alpha$  .

Based on fully-open slit observations of spectrophotometric standards.

than [N II] and [S II] . The H $\alpha$  line is also comparable to or more extended spatially than the other four emission features. Addition of these lines would only marginally improve the rotation curve solutions, and they were left out for simplicity. In this paper, we will thus focus solely on the reduction of H $\alpha$  RCs.

## 2.1. Basic Procedures and Geometrical Corrections

Steps were taken to assemble the appropriate calibrations to transform CCD frames from a distorted row-column pixel space to an orthogonal wavelength-spatial map. The CCD frames were then re-binned on a regular spacing grid and re-sampled such that wavelength and radial increments are constant within each bin. Standard calibration material includes high signal-to-noise dome flats (with same slit opening as galaxies) and a series of short (bias) and long dark frames. No twilight flats were taken. He-Ne-Ar comparison lamp exposures were taken at the beginning and end of each night, and the wavelength calibration zero-point was determined directly from the night emission skylines. The line-curvature was mapped from the calibration spectra whereas “S-distortion” mapping was modelled directly from the galaxy’s continuum.

## 2.2. Preliminary Reductions

The baseline level (DC offset) was removed as in Paper I. We also mapped and removed the fixed-pattern noise along the slit direction due to uniform dark current. All the images were divided by a map of the pixel-to-pixel sensitivity variations in the detector. The noise-variance frames described in §3.2 were measured prior to flat-fielding to exclude contributions from the dome, sky, and scattered-light backgrounds. This ensures proper error propagation. CCD images were also corrected for cosmetic defects. Hot pixels and bad columns were replaced by a local second-order polynomial fit. Automatic cosmic-ray rejection requires more delicate attention, especially near emission lines. Cosmic rays hits are usually more compact than real spectral features but an uneven overlap of two or more such events will easily mimic localized emission features. Cosmic ray removal was thus performed interactively.

The “S-distortion” was finally removed from all the bias-subtracted and flat-fielded frames via inverse-shifting of a smooth model from the galaxy continuum. The amplitude of this distortion at the slit center varied from 1 to 3 pixels across the full spectral range. The baseline, dark subtraction, flat-fielding, removal of cosmetic defects, and correction for S-distortion were all done (in that order) in batch mode using custom procedures in VISTA.

## 2.3. Wavelength Calibration and Line-Curvature

A polynomial pixel-wavelength fit was extracted from each He-Ne-Ar calibration spectrum using interactive line identification. Eight to thirteen unblended lines were identified in each of the lamp spectra, and a third-order polynomial was fit to derive a dispersion curve. The rms residuals in the wavelength solution were of the order of 0.05 pixel, which corresponds to 0.051 Å and 0.076 Å (or about 2.5 km s<sup>-1</sup> at H $\alpha$ ) for Lick and Las Campanas data respectively. The precision of most centroiding programs is only about 1/20<sup>th</sup> to 1/40<sup>th</sup> of a pixel, and 0.05 pixel residual is thus satisfactory. Barring zero-point flexure shifts, the dispersion solutions were very stable over a run. The same calibration lamps were used to model the effects of line-curvature. The spectra were re-binned along the dispersion axis into a logarithmic wavelength scale to provide equal velocity interval per pixel. An example of a flat-fielded and rectified spectrum is shown in Fig. 1 for UGC 1437.

We used position angles listed in the Uppsala Catalog of Galaxies (UGC) to align the slit of the spectrograph with the galaxy’s major axis. These were found to be in excellent agreement ( $\pm 1^\circ - 4^\circ$ ) with our measured values from *r*-band CCD surface photometry (Paper I).

### 3. Extraction of RCs

Extraction of a final rotation curve requires a few more steps; zero-point adjustment of the dispersion solution for flexure shifts, construction of a noise-variance map, identification of the galaxy’s center, sky subtraction, and removal of night-sky emission lines and galaxy continuum,

Tests using a cross-correlation approach to determine the center of the galaxy automatically showed that the choice of a good template is critical. The center of bright late-type spirals usually shows strong lines of  $H\alpha$  and weaker  $[N II]$  pair. Since a number of those exhibit  $H\alpha / [N II]$  reversal in their center<sup>6</sup>, we opted for an interactive intensity-weighted marking of the center. It is still difficult to define a true dynamical center using this technique since the strength of the emission lines does not necessarily correlate with the depth of the central potential. Moreover, 20% of the sampled galaxies showed no continuum and/or nuclear emission. In such cases, an eyeball estimate of the center was made. A more reliable galaxian center was redefined via parametric modeling of the map of velocity centroids (see §5).

To quantify and correct for the effects of flexure, the 2D spectra were first binned on a linear wavelength scale (with line curvature taken into account) to extract a spectrum of the night-sky airglow from the galaxy sky background. The zero-point of the dispersion solution was obtained by comparing the skylines of Ne I and OH transitions with a list of reference wavelengths (Osterbrock & Martel 1992). The effects of flexure shifts on the relative measurement of RCs are completely negligible but the redshifts themselves are directly affected. Gravity and telescope motion can contribute absolute shifts as great as 4 pixels.

The skylines and sky background were removed by interpolating the regions above and below the galaxy emission with a second-order polynomial. In few cases where the galaxy was too extended and filled the slit, we interpolated the sky spectrum from both sides of the  $H\alpha$  emission complex ( $H\alpha + [N II]$ ). An example of skyline and sky background subtraction is illustrated in Fig. 2.

Last, galaxy continuum or, more generally, all the uniform structure parallel to the dispersion axis (*e.g.* stars on major axis) must also be removed. This operation is useful for a closer interactive determination of the galaxian center where continuum and emission lines intersect. To do this carefully (especially around the  $H\alpha$  emission complex), we shifted the data by the inverse of a coarse (integer) model of the rotation curve so that the galaxy emission lines all become straight (to within a fraction of a pixel). The background was fitted row-by-row and subtracted from

---

<sup>6</sup>The strength of this effect varies upon the amount of nuclear and disk light which enters the slit aperture (Rubin & Ford 1986, Storch-Bergmann 1991). A quantitative model to predict the strength of this  $H\alpha / [N II]$  reversal is still missing. The effect has been noticed for several decades, but there has not been enough information to choose between viable explanations. Collisional and photo-excitation could play a role, but intrinsic variations in core abundances are also possible. Preliminary results from our data also show that spirals with bigger bulges and rapidly rising RCs (early-type spirals) exhibit stronger “reversals”.



the data. The images were then shifted back to recover their exact pre-subtraction configuration (see Fig. 5.3). Integral shifts ensure that no spectrum degradation was introduced. Finally, a noise-variance was constructed for each galaxy spectrum to allow the measurement of velocity errors (C92).

We measured the intensity-weighted centroids at each row along the  $H\alpha$  galaxy emission using a parabolic-binned interpolation (see Appendix C). This technique makes no assumption about the profile shape and as such, yields both a robust center and error estimate.

The signal-to-noise threshold was chosen to represent an error of a third of a pixel in the determination of the centroid. This corresponds roughly to  $S/N < 5$  or a velocity error greater than  $16 \text{ km s}^{-1}$  at Lick and  $25 \text{ km s}^{-1}$  at Las Campanas.

The final set of CF ORCs is shown in Appendix A. Figure 4 shows the distribution of the maximal extent of ORCs scaled by the disk exponential scale length  $h$ .

#### 4. Comparison with Other Work

We now compare our results with the series of photographic ORCs by Rubin and coworkers (Rubin *et al.* 1985, and references therein). Rubin’s sample does not probe the extragalactic volume as deeply as ours and includes earlier types. Consequently, the overlap between our samples is limited to 8 galaxies, as shown on Fig. 5. Rubin’s smoothed two-sided RCs (represented by open squares) were scanned and digitized from old paper tracings kindly provided to us by Vera Rubin. Our data (filled circles) are not smoothed and hence display larger fluctuations. Most detections (and non-detections) and overall shape variations are well matched. Our RCs for U1550 and U5250 are slightly shallower but this is explained by a shorter exposure time than normal.

Good agreement is also found with 3 galaxies from MAT’s collection, as seen in Fig. 6.

The thesis sample of Vogt (1994) offers a more substantial overlap. This is shown in Figs. 7a,b. Vogt’s sample, observed with the Palomar 5m, was designed to probe the fainter ends of RCs to study environmental effects in clusters. Longer integration times and the aperture ratio both account for greater  $S/N$  in Vogt’s data. In most cases though, the physical extent and broad features between Vogt’s data and ours compare favorably. Typically, detection of nebular  $H II$  emission via long-slit spectroscopy is limited to a common isophotal radius (see Fig. 4) for nominal TF exposures times ( $< 2000\text{s}$  on 5-m class telescopes). The 23 RCs shown in Fig. 7a,b are reasonably smooth and show little deviation from circular motions. Vogt’s data show kinematic “twists” for U1437 and U12631 which are not confirmed by our data (nor are they challenged either; here, comparisons suffer from non-detections.)

Fabry-Perot (FP) spectroscopy offers significant advantages over conventional long-slit spectroscopy for the extraction of optical RCs (cf. *e.g.* Schommer *et al.* 1993). First, the velocity field is fully mapped spatially. This yields greater  $S/N$  in the outer regions and provides a

more robust measure of the galaxian circular velocity. Second, deprojection of the velocities uses kinematical information directly instead of photometric inclinations for long-slit data which may not be adequate (Schommer *et al.* 1993). Comparison with the H $\alpha$  FP data of Amram *et al.* (1992, 1994) is nonetheless quite satisfactory on large scales (Fig. 8). The FP profiles (open squares) consist of a smooth rotation curve projected on the plane of the sky. They extend much farther out and show less small scale noise than our major-axis cuts (filled circles). The localized perturbations on the major axis are attributable to spiral arms and non-circular motions. Still, we tested that linewidth measurements from smooth fits of long-slit RCs are in close agreement with similar linewidths from FP ORCs. FP data cubes require a few hours of on/off integrations on large telescopes (> 4-m) which makes any FP investigation of a large sample of galaxies logistically challenging. While we recognize the merits of FP data over long-slit spectra, it is believed that the latter can still provide sufficient S/N and sampling to measure the most representative value of circular velocity for the galaxy.

## 5. Modelling the Rotation Curve

Before we derive various measures of rotation velocities from ORCs, it is worth considering different parameterizations or models which might best describe their shape. A disadvantage of this approach is that *a priori* assumptions about the shape of the RC must be made. The major advantage is that all points (and their errors) are used simultaneously and systematic deviations in defining a robust linewidth measure are likely to be reduced. We will see below that “model” linewidths prove to be most reliable.

*Physical* modelling of RCs is not a simple affair since it requires a complete description of the contributions from the bulge, disk, and (bright and dark) halo components to the overall galaxy dynamics. Such global models have been proposed, first with the Keplerian formulation of Brandt (1960, and references therein) and culminating recently in the “Universal Rotation Curve” (URC) of disk galaxies by PSS which accounts for luminous and dark matter. One wishes to adopt a parameterization which most naturally espouses the shape of each RC, with no pretense of having a physical basis, yet with the least number of free parameters. Use of a smooth rotation curve model will allow for the measurement of specific rotational speeds (metric, isophotal, etc.) and, in principle, extrapolation of the original data if they do not extend beyond a certain fiducial radius.

Three models were tested: 1) a basic 2-parameter arctan function, 2) a more elaborate *ad-hoc* fitting function, and 3), the “URC” parameterization of PSS. Models 1 and 2 were fitted using a Levenberg-Marquardt technique. Application of Model 3 only required input of 2 variables, the absolute luminosity and the optical radius of the galaxy. The models were applied to both CF and MAT ORCs (projected on the plane of the sky.) The fits for all observed CF spectra are reported in Appendix A (on top of the actual data), and the fit coefficients for both CF and MAT data are given in Appendix B. Plots and models for MAT’s data are available from the author upon request.

It is useful to gauge galaxy sizes in terms of an optical radius and we adopt below the definition of PSS for a pure exponential galaxy:  $r_{opt} \equiv 3.2h$ , where  $h$  is the disk exponential scalelength (Paper I). More generally,  $r_{opt}$  is defined as that radius which encloses 83% of the total light. It is closely equivalent to the isophotal radius at 24  $r$ -mag/arcsec<sup>2</sup>,  $r_{24}^c$  (Paper I). We also write  $V_{opt} \equiv V(r_{opt})$ .

### Model 1. The ARCTAN function

The normalized arctan RC fitting function is given by:

$$v(r) = v_0 + \frac{2}{\pi}v_c \arctan(R), \quad (1)$$

where  $R = (r - r_0)/r_t$ ,  $v_0$  is the velocity center of rotation,  $r_0$  is the spatial center of the galaxy,  $v_c$  is an asymptotic velocity, and  $r_t$  is a transition radius between the rising and flat part of the RC. This function reproduces the shape of RCs reasonably well with the smallest number of arguments. Moreover, it emerges naturally from the standard parameterization of dark halo density profiles (cf. *e.g.* Gilmore, King, & van der Kruit 1990, p.212). The arctan model is shown in Fig. 9 for various values of  $r_t$  and  $v_c = 200 \text{ km s}^{-1}$ . Arctan fits for all galaxies are plotted in Appendix A as long-dashed curves on the folded RCs. The curves are often hidden under the continuous line which describes model 2 below. The arctan model provides an adequate match to most RCs, does not account for any sharp peak near the turnover radius (*e.g.* U3181, U7337, U8161). It does handle sharp transitions and changing slopes fairly well, from “boxcar” profiles (*e.g.* U10621) to slowly rising curves (*e.g.* U11606, U12304). The fit parameters for each CF ORC are given in Appendix B, Table A2.1. A similar list for MAT ORCs is presented in Appendix B, Table A2.2. Note that  $v_c$  can be arbitrarily large especially for small values of  $r_t$ . Thus, it should not be considered as a useful definition of a galaxy’s rotational linewidth (cf. *e.g.* Schlegel 1995).

### Model 2. The Multi-Parameter function

A more elaborate, purely empirical formulation is:

$$v(r) = v_0 + v_c \frac{(1+x)^\beta}{(1+x^\gamma)^{1/\gamma}}, \quad (2)$$

where  $x = 1/R = r_t/(r - r_0)$ , and  $v_0$ ,  $r_0$ ,  $v_c$ , and  $r_t$  are defined as above in Model 1 but  $v_c$  and  $r_t$  do not take the same values. Solid-body rotation, or  $v(r) \propto r$  (with  $\partial v/\partial r \sim v_c/r_t$ ), is recovered for  $|r - r_0| \ll r_t$ , and flat rotation, or  $v(r) \propto v_c$ , is achieved for  $|r - r_0| \gg r_t$ . Similar formulations have also been developed by Schlegel (1995), Rix *et al.* (1997) and Kravtsov *et al.* (1997). The term  $\gamma$  governs the degree of sharpness of turnover, and  $\beta$  can be used to model the drop-off or steady rise of the outer part of the RC, mostly for systems with a fast solid-body rise. Barring zero-point offsets, this function uses 3 main fitting parameters:  $v_c$ ,  $r_t$ , and  $\gamma$ . The term  $\beta$  was used for 30 of the 304 CF galaxies; it is normally set to zero in first iterations. We used only  $\beta$  for 16 of MAT’s 958 modelled RCs.

A representation of typical models is shown in Fig. 10 for a range of shape parameters,  $\gamma$ , at a given  $v_c$  and  $r_t$ . The effect of varying  $\beta$  is also illustrated (dotted lines). For given values of  $v_c$  and  $r_t/r_{opt}$ , the multi-parameter fit with  $\gamma = 1.1$  reproduces the arctan fit almost identically. RCs with larger  $\gamma$ 's are not as well matched by the arctan. The best match of Model 2 to each RC is shown as a solid line in Appendix A. The fit parameters for CF and MAT galaxies are again listed in Appendix B.

The success of Model 2 is immediately obvious upon visual examination of the fits. Figs. 11a-d show the difference  $\chi^2(\text{mp}) - \chi^2(\text{at})$  between the multi-parameter (Model 2) and arctan (Model 1) fits, against  $r_t$  and  $\gamma$  (both from Model 2) for CF and MAT galaxies. A preponderance of negative differences favors the multi-parameter fitting function; statistical equivalence is achieved for  $|\Delta\chi^2| \leq 1$ . An  $F$ -test further reinforces the greater confidence level (of order a few sigmas) of Model 2 over Model 1, especially for MAT galaxies. The  $\chi^2$  differences are either insignificant or reversed at small values of  $\gamma$  for rising RCs. Model 2 also suffers from obvious coupling between  $r_t$  and  $\gamma$ , especially for small values of  $r_t$  and  $\gamma$ . Fig. 12 highlights the strong covariance that exists for  $r_t/r_{opt} \leq .3$  and  $\gamma \leq 2.5$ . As expected, slow rising RCs (fainter galaxies) are favored by a model with a low  $\gamma$  and high  $r_t/r_{opt}$  as seen in Fig. 12. Model 1 offers a reasonable match for galaxies with  $\gamma \leq 1.5$ . It is, however, less adequate for the brighter galaxies with greater  $\gamma$ 's. The differences are most striking for rising or declining RCs in their outer parts and sharply rising curves in their inner parts (often associated with strong central concentrations).

Model 2 fits a greater panoply of RC shapes and shall be adopted below. Because of internal coupling, Model 2 should be avoided in analyses of galaxian structural parameters. a

### Model 3. The Universal Rotation Curve (URC)

The ‘‘Universal’’ parameterization of PSS has recently been used as a tool to model TF velocities (G97). PSS’s physical model was designed to account broadly for the contribution of the luminous and dark matter to the overall RC. In its current form, luminous matter is modelled from the contribution of a stellar exponential thin disk and the dark matter halo is expressed as an isothermal sphere. The dark component is scaled by assuming a maximum (luminous) disk. This parameterization implies that all the families of RC shapes can be characterized by luminosity alone. The URC uses two variables as input:  $L$ , the absolute blue luminosity of the galaxy<sup>7</sup>, as the shape parameter and the optical radius  $r_{opt}$  for normalization at  $V_{opt}$ . Equation 14 of PSS is written as:

$$V_{URC}(x) = V(r_{opt}) \left[ \left( 0.72 + 0.44 \log \frac{L}{L_*} \right) \frac{1.97x^{1.22}}{(x^2 + 0.78^2)^{1.43}} + 1.6 e^{-0.4(L/L_*)} \frac{x^2}{x^2 + 1.5^2 (L/L_*)^{0.4}} \right]^{1/2} \text{ km s}^{-1} \quad (3)$$

with  $x = r/r_{opt}$ .

---

<sup>7</sup>We explicitly drop the  $B$ -band subscript for consistency with the PSS notation.

We use  $M_B^* = -20.5$ , *i.e.*  $\log L_B^* = 10.4L_\odot$ , in concordance with PSS<sup>8</sup>.

Since derivation of the galaxy luminosity is the final product of the TF machinery, using a luminosity-dependent formula for TF applications, such as that of PSS, requires an iterative procedure to solve for the final metric. We allow ourselves to violate this argument by using measured  $L_B$  from the RC3 for the sake of verification. Color transformations to convert available  $r$ -band luminosities (Paper I) to the  $B$ -band are avoided to minimize errors. URC models are only computed if both  $r$ -band and  $B$ -band luminosities are available. Moreover, these models can only be computed if surface photometry exists to estimate  $r_{opt}$ , either directly or from the scale length for pure disk galaxies. Photometry must also extend beyond  $r_{opt}$  ( $\equiv 3.2h$ ).

The subjectivity in choosing proper scale lengths or applying an exact fraction (83%) of the “total” light to measure  $r_{opt}$  provides an additional source of uncertainty for those models. Besides being model dependent,  $r_{opt}$  increases with wavelength due to extinction effects (Burstein, Willick, & Courteau 1994). Care must thus be taken when applying the URC in different wavelength regimes. We make no compensation for dust effects at this point.

URC models were computed for 131 galaxies and are compared to the data in Appendix A; these are represented with a dotted curve.

A visual classification scheme suffices to assess the goodness of fit; 70 models were rated “good”, 21 “marginal”, and 40 were labelled “poor”. This degree of success ( $> 50\%$ ) is perhaps satisfactory for broad galaxy formation and scaling issues but is less adequate for accurate modelling and TF applications (as has been recognized by PSS). The URC fails most conspicuously for rapidly rising curves and seems to predict too strong a decline in the outer regions. In the bulge region, the PSS model has a tendency to overshoot a slow solid-body rise and underestimate any fast rise. This is readily understood by the absence of a bulge term in the URC formulation. While central regions of late-type systems may be small and faint (Courteau, de Jong, & Broeils 1996), their contribution to the gravitational potential is non-negligible (Broeils & Courteau 1998). Furthermore, the circular complication involved in using luminosities as input in the URC formula prevents any direct TF application. Issues involving the choice of blue luminosities (which are strongly affected by dust), a wavelength- and model-dependent definition (isophotal radii or scalelengths), adjustment of internal constants ( $L_B^*$  and  $H_o$ ), and revision of the distribution of light to include a bulge component, all need to be addressed in a more comprehensive analysis. In its present form, the URC should not be used for exact modelling. Extrapolation of the URC to estimate  $V_{opt}$  for shallow RCs is equally admonished in light of the potentially large data-model differences in the outer parts (cf. Appendix A).

In what follows, we adopt Model 2 as the best parameterization to describe ORC shapes for

---

<sup>8</sup> Both the Stromlo-APM survey (Loveday *et al.* 1992) and recent results from SSRS2 (Marzke *et al.* 1997) for spiral galaxies suggest that  $M_B^* = -19.5 + 5 \log(H_o/100) = -20.1$ , or  $\log L_B^* = 10.2$  for  $H_o = 75$ . The offset between this and PSS’s value will cause model departures at the 2-3% level.

the TF work. Model 1 may prove more useful for structural analyses.

## 6. Rotational Velocities for TF Use

The TF relation is based in part on an estimate of the “intrinsic” rotational speed, or linewidth, of a disk galaxy which is measured beyond the central rise of the RC. The definition of linewidth varies from author to author. Linewidth measurements with respect to peak levels of the 21-cm “horned” profile were initially favored for computational simplicity. However, peak intensities are affected by sampling and binning effects. Modern linewidth measurements are based on robust quantities such as integrated flux or mean intensity (*e.g.* Bicay and Giovanelli 1986) or the slope of the profile edges (*e.g.* Bottinelli *et al.* 1983).

Since HI linewidths have defined the standard for most TF calibrations to date, it is appropriate to seek a new definition of optical rotation which will *best reproduce 21cm results*. This new optical linewidth should also meet two basic requirements: *best internal scatter* (*i.e.* robust to observational errors) and *minimization of TF residuals*. A similar search was undertaken by Raychaudhuri *et al.* (1997) but their small sample as well as the lack of repeat observations prevented them from discriminating among their various linewidth measures. They were able to confirm that ORCs yield as small a TF scatter as H I linewidths (see §11).

The measurement of linewidths from resolved RCs is advantageous since emission line centroids are not affected by internal and instrumental broadening. However, with increasing distance, seeing effects become important and the shape of RCs can be significantly altered near the center (*cf. e.g.* Vogt *et al.* 1996). At higher redshifts ( $z > 1$ ), the velocity field of a distant galaxy may completely fill the entrance aperture of either long-slit spectrographs or integral field units. It is thus important to keep track of calibrations based on integrated rotation profiles as well as resolved RCs to allow a bridge between TF calibrations at low and high redshifts.

### 6.1. Linewidths from Resolved Rotation Curves

Various measures to estimate the maximum rotational speed from an asymmetric and noisy rotation curve are investigated below. Those based on only a few velocity points are expected to reproduce rather poorly. C92 tested 3 linewidth measurements,  $\Delta V_{max1}$ ,  $\Delta V_{max2}$ , and  $\Delta V_{max3}$ , based on the 1st, 2nd, and 3rd highest velocity points on each side of the RC. An average of these,  $\Delta V_{123}$ , was also computed (see §7).

### 6.1.1. Weighted Mean Method

A less susceptible approach consists of taking the weighted mean of all the velocity points where the RC levels off. We do this by summing 20% of all the velocity points from the far-end of the ORC on each side. For a fast rotator, this is equivalent to drawing a line through the points on the rotation plateaus. The mean of the summations on both sides is  $\Delta V_{box}$ . R97 describe this method in their §4.3. This technique suffers mostly from an ill-defined interior boundary of integration. The weighted-mean method most closely matches the eye-ball technique of MAT to fit optical line widths. The subjective nature of this method makes duplication and testing of MAT’s results virtually impossible.

### 6.1.2. Model Linewidths

We define more objective and stable measures of TF velocity based on the ORC parameterization (Model 2) in conjunction with, in some cases, photometric parameters. Four measurements were examined: i)  $V_{max}$ , the peak velocity of the model, ii)  $V_{2.2}$ , the velocity interpolated at  $r_{disk} = 2.15$  disk scale lengths which corresponds to the location of peak rotational amplitude for a pure exponential disk (cf. *e.g.* Freeman 1970, Binney & Tremaine 1987, Courteau & Rix 1997), iii)  $V_{opt}$ , the velocity measured at  $r_{opt}$ , and iv)  $V_{iso}$ , an “isophotal” velocity inferred at the 23 mag/arcsec<sup>2</sup> isophotal level (cf. Paper I).

## 6.2. Linewidths from Integrated Velocity Profiles

We now explore alternative linewidths from integrated profile which resemble single-dish 21cm spectra. This is done by adding all the velocity points which define the ORC along the spatial axis of the galaxy. The motivations for studying this technique are twofold: 1) its principles are based upon a well-proven method (radio linewidths), and 2) a calibration (intensity-weighted) will be necessary for investigations of unresolved rotation profiles from high-redshift galaxies (Courteau, Sohn, & Faber 1998). The most important benefit of histogram measurements is the increase in linewidth S/N since *all* the velocity points are used in the computation.

Two velocity histograms are of potential interest: the *un-weighted* and *intensity-weighted* cases. The major weakness of *intensity-weighted* profiles is that a flux integral will favor the brightest H II regions (Schommer *et al.* 1993, R97). This effect is still sufficiently mild in normal spirals (*i.e.* non-starburst, LINERs, or Seyfert galaxies) that a TF calibration can still be defined (*e.g.* C92 and below). *Un-weighted* velocity histograms alleviate this shortcoming entirely.

### 6.2.1. *Un-Weighted Histograms and Probable Linewidths*

One can sort all the velocity data points (which obey the minimum S/N criterion) and calculate the difference,  $W_{hist}$ , between the 10<sup>th</sup> and 90<sup>th</sup> (interpolated) percentile points in the ranked distribution of velocities. This technique, first used by Dressler & Faber (1990) and further developed by Vogt (1994), is similar to constructing an unweighted velocity histogram and measuring the width at 10% of total area on each side of the profile. A variant of this technique called the “Probable Min-Max” (PMM) method by R97 (see their §4.6), considers the probability distribution of all velocity points with their Gaussian errors. A velocity  $W_{prob}$  is computed from the difference of the 90% probable maximum and minimum from both sides of the RC. This method is however sensitive to broadening effects which are reflected in the velocity error at each point.

### 6.2.2. *Intensity-Weighted Histograms*

We explored three flux-weighted linewidth measurements:  $W_{15}$ ,  $W_{20}$ , and  $W_{25}$ . The area under each profile is measured by integrating along the velocity axis; fractional flux levels are computed via parabolic-binned interpolation (see Appendix C). We define a velocity linewidth,  $W$ , as the difference between those velocities where the integration reaches a predefined percentage of the total area, *e.g.* 10% and 90% for  $W_{20}$ . Definitions relative to peak intensities are avoided since the detailed shape of the profile is sensitive to spectral resolution and, for ORCs, to the individual fluxes of H II regions lying on the slit. While the exact shape of the profile is not a conserved quantity, its area or total flux, should be. Fig. 13 shows the locations of these width markers for UGC1437. These are measured quite high compared to 21cm profiles (*cf.* *e.g.* Roberts 1978, Bica & Giovanelli 1986). A discussion of this choice of optical linewidths and systematic effects will be given in Courteau, Sohn, & Faber (1998).

We consider one last measure of integrated linewidth,  $W_{50m}$ , the separation between the velocity points where the intensity reaches 50% of the mean flux over the full velocity range of detectable signal. This is analogous to 21cm linewidths defined at 50% of the total mean.

Rotation profiles for each galaxy were not presented for space considerations but are available at request from the author.

## 6.3. **Logslopes**

For future use, we also compute the logarithmic slope,  $d \log v(r)/d \log r$ , from the folded deprojected data in the rest-frame of the galaxy. Measurement of logslopes from sparse data is



exceedingly sensitive to noise and we use a bootstrapping technique<sup>9</sup> to infer their mean and error. The mean logslope of the observed data,  $ls_r$ , is computed between  $r_{disk}$  and the last measured velocity point. We also compute an analogous quantity,  $ls_m$ , from Model 2. These are given in Table 13.

Fig. 14 displays the distribution of logslopes,  $ls_r$  and  $ls_m$ , for all CF galaxies. About 4% of the sample exhibits declining outer slopes and  $\sim 60\%$  of all RCs have achieved convergence, *i.e.*  $ls_r \leq 0.2$ . This fraction of convergent profiles is lower than the 81% found by Schlegel (1995) for a sample of 282 nearby IRAS-selected galaxies. None of Schlegel’s RCs exhibit negative logslopes either. This high rate of convergence of IRAS-selected galaxies, if true, is surprising since the TF scatter for these galaxies was found to be higher than for optically-selected spirals (Schlegel 1995). One would expect that better behaved linewidths (*i.e.* more convergent profiles) would yield reduced TF scatter. Massive star formation activity characteristic of IRAS galaxies could however bias the luminosity high and explain Schlegel’s observations. van Driel *et al.* (1995) also studied TF differences between optically-selected and IRAS galaxies but did not find striking discrepancies. Further investigations of IRAS-galaxies would be desirable, especially if their RCs are systematically flatter than ORCs as indicated by their logslopes.

## 7. Internal Errors from Repeat Measurements

We have measured repeatability errors from multiple observations of 62 galaxies, for a total of 132 independent observations. These are all reported in Appendix A. Unweighted standard deviations,  $\langle \sigma_{obs}^2 \rangle^{\frac{1}{2}}$ , in  $\text{km s}^{-1}$  are given in Table 2 below for the various linewidth measures. These refer to the one-sided value of the rotational velocities (*i.e.*  $\Delta V/2$ .)

Not surprisingly, all measures of linewidth based on one or a few velocity points fare rather poorly. The “box” method shows improved internal errors purely for statistical reasons. This technique is equivalent to fitting the best horizontal line through the flat rotation curve.

Internal errors for all model linewidths and the velocity histograms are small and hold great promise for TF analysis. Errors above  $8 \text{ km s}^{-1}$  are unsatisfactory and suggest that the linewidth measure is too sensitive to observational errors. Of the linewidths with smallest internal scatter,  $V_{2.2}$ ,  $V_{opt}$ , and  $V_{iso}$ , are however photometry-dependent. The linewidth with best internal scatter,  $W_{hist}$ , also holds the distinction of being completely independent of any modelling of the RC or scaling via photometric parameters. Its operational simplicity also makes it ideal for widespread use.

The three raw linewidths,  $W_{15}$ ,  $W_{20}$ , and  $W_{25}$  all show internal scatter comparable to those

---

<sup>9</sup>We use linear least-square fitting on a random selection of all the velocity points included in the fit. This operation is repeated 100 times. A logslope is computed if at least 6 velocity points are available. Otherwise, it is set to zero.

Table 2  
RMS Error of a Single Observation for *Raw* Velocity Parameters

	$\Delta V_{max1}$	$\Delta V_{max2}$	$\Delta V_{max3}$	$\Delta V_{123}$	$\Delta V_{box}$	$V_{max}$	$V_{2.2}$
std. dev.:	15.3	8.5	7.7	10.0	7.0	6.6	5.7
	$V_{opt}$	$V_{iso}$	$W_{hist}$	$W_{prob}$	$W_{15}$	$W_{20}$	$W_{50m}$
std. dev.:	5.7	5.6	5.5	8.3	5.9	6.3	12.6

quoted for radio velocity widths (Bothun *et al.* 1985, Freudling 1990, Mould *et al.* 1993). The errors on  $W_{50m}$ , which samples the optical profile lower in the wings, are too large to make it a good velocity width indicator. We found no correlation between linewidth error and distance (redshift) or absolute luminosity (linewidths).

## 8. Corrections to Linewidths

Observed line-of-sight velocity widths, whether they are measured from resolved RCs or integrated profiles, must be corrected for projection on the sky and cosmological stretch. The corrected rotation width,  $W_c$ , is

$$W_c = \frac{W_{raw}}{(1+z)\sin i} \quad (4)$$

where the observed *raw* linewidth,  $W_{raw}$ , must be treated for various broadening effects prior to deprojection *if* the widths are derived from an integrated spectrum. A potential source of error for resolved linewidths is that of slit misalignment. To test this, we rotated the slit at various position angles spanning a range of  $8^\circ$  on a few test galaxies. Results showed no discernible effect. Giovanelli *et al.* (1997) also simulated this effect and report negligible errors for PA offsets less than  $15^\circ$ .

Corrections to integrated profiles must account for broadening effects such as instrumental resolution and focus variations, “turbulent” (non-circular, perpendicular) motions of the gaseous component, signal-to-noise of the spectrum, and smoothing. Instrumental resolution and focus variations were accounted for by measuring the width of OH emission-lines at the same height as that measured on the galaxian integrated profiles (see Table 1 for representative values.)

Since the full width is a convolution of the true profile of the galaxy with that of the instrument, we assume that

$$W_{raw}^2 = W_{galaxy}^2 + W_{resolution}^2 \quad (5)$$

This is strictly true for Gaussian profiles, but tests show that it seems to work adequately for

double-peaked profiles as well. The typical contribution of instrument and focus broadening to the final width is  $\sim 5\%$  for fast rotators ( $V_{max} > 200 \text{ km s}^{-1}$ ) and  $\sim 9\%$  for slow rotators ( $V_{max} \leq 200 \text{ km s}^{-1}$ ). Focus variations ( $\sigma_f \sim 10 \text{ km s}^{-1}$ ) contribute less than a percent to the overall width.

A correction for turbulence was derived by Tully & Fouqué (1986; hereafter TF86), based on the earlier treatment of Bottinelli *et al.* (1984). Eq. 12 from TF86 assumes that the raw linewidth,  $W_{20}$ , is already corrected for instrumental resolution effects. Application of this formula would not be strictly adequate here since we have not demonstrated equivalence between their  $W_{20}$  and our linewidths corrected for instrumental broadening. Independent investigations (Rhee & Broeils 1997) suggests that TF86’s formulation slightly overestimates the broadening effects of turbulence (which itself is a rather poorly constrained phenomenon), but regardless of the exact treatment, this correction is small for the large galaxies considered here. We chose to neglect it in our treatment. Moreover, unlike instrumental broadening, turbulence does not affect the TF scatter and therefore, should not alter our conclusions.

The inclinations were estimated using CCD ellipticities,  $\varepsilon$ , and assuming an intrinsic flattening ratio,  $q_0$ , of 0.18 for all the galaxies (see Paper I for a discussion on the choice of ellipticities). We use

$$\cos^2 i(\varepsilon) = \frac{(1 - \varepsilon)^2 - q_0^2}{1 - q_0^2}. \quad (6)$$

where the ellipticities for each galaxy are given in Table 4. Slightly different estimates for the flattening parameter,  $q_0$ , are quoted in the literature; for disk galaxies, these vary between 0.11 to 0.20 (see *e.g.* Haynes & Giovanelli 1984, B85, Han 1991, Willick 1991, Rhee 1996, G97). Variations in the choice of  $q_0$  have very little effect on the projection correction of the velocity width (col. 3) due to the slow variation of the sine function for large inclinations (where  $(1 - \varepsilon)$  becomes comparable to  $q_0$ ); the inclination-dependent correction for internal extinction is also very little affected by the precise choice of  $q_0$  since it is assigned a fixed value for  $i > 80^\circ$  (see Paper I). For  $\varepsilon \geq 0.82$ , where inclination measurements become limited by the intrinsic thickness of the disk, the inclination value was set to  $90^\circ$ . Inclinations are in principle affected by atmospheric seeing (*e.g.* Saglia *et al.* 1993, G97) but the seeing disk is small compared to the size of our galaxies. Our sample is limited to  $i \leq 75^\circ$  where seeing effects are reduced.

## 9. Presentation of the Data

We present in Table 3 a list of the main measured spectroscopic quantities for all the CF galaxies. In cases where a galaxy was observed more than once, the measurements are an unweighted average. All the velocity widths are corrected for inclination and redshift broadening following Eq. 4. Integrated linewidths (only  $W_{15}$  and  $W_{20}$  are presented here) are also corrected for instrumental and turbulent broadening. All the linewidths show twice the galaxian rotation. In cases where *model* linewidths could not be measured due to shallowness of the RC, the velocity

is listed as zero. Recall finally that logslopes are computed from deprojected velocities. Only the first page of this table is shown here. Table 3 is arranged as follows:

- Col. (1): UGC number of the galaxy. The last two entries refer to CGCG reference numbers (cf. Paper I for PCG numbers);
- Col. (2):  $n$ , the total number of observations per galaxy;
- Col. (3):  $i$ , the inclination of the galaxy in degrees calculated with Eq. 6 from ellipticities given in Paper I. An intrinsic flattening of 0.18 is assumed;
- Col. (4):  $cz_{LG}$ , the radial velocity corrected for motion with respect to the Local Group,  $cz_{LG} = cz_{\odot} + 300 \sin(\ell) \cos(b)$ . The heliocentric redshift,  $cz_{\odot}$ , is defined as the center of symmetry of the rotation curve as measured with Model 2 (cf. Paper I);
- Col. (5):  $cz_{CMB}$ , the radial velocity in the frame of the Cosmic Microwave Background. The correction uses the motion of the Sun with respect to the CMB frame determined by the COBE dipole anisotropy (Kogut *et al.* 1993);
- Col. (6):  $W_{15}$ , the velocity width measured from the flux-weighted rotation profile at 15% of the total area;
- Col. (7):  $W_{20}$ , same as  $W_{15}$  but measured at 20% of the total area;
- Col. (8):  $V_{max}$ , the peak velocity from the fitted RC with Model 2;
- Col. (9):  $V_{2.2}$ , the velocity from Model 2 measured at  $r_{disk} = 2.15h$ , where  $h$  is the disk scale length from 1D bulge-to-disk decompositions (cf. Paper I);
- Col. (10):  $V_{opt}$ , the velocity from Model 2 measured at  $r_{opt} = 3.2h$ , the optical radius defined as in PSS;
- Col. (11):  $W_{hist}$ , the velocity difference between the 10<sup>th</sup> and 90<sup>th</sup> (interpolated) percentile points in the ranked distribution of velocities;
- Col. (12):  $W_{prob}$ , the velocity difference between the probable minimum and maximum of the RC at the 90% level (cf. R97);
- Col. (13):  $ls_m$ , the logslope measured from Model 2 between  $r_{disk}$  and the last fitted velocity point;
- Col. (14):  $ls_r$ , the logslope measured from the observed RC between  $r_{disk}$  and the last measured velocity point;
- Col. (15):  $D$ , the distance of the galaxy in Mpc,  $D = cz_{LG}/H_0$ ;

Col. (16):  $r_{max}$ , the maximum spatial extent in arcseconds of either the approaching or receding side of the galaxy spectrum;

Col. (17):  $r_{kpc}$ , same as above but in units of kpc.

Col. (18):  $m_c^r$ , the corrected  $r$ -band total apparent magnitude from Paper I, which here also includes a small  $K$ -correction term (cf. Willick *et al.* 1997, Eq. A14);

Col. (19):  $M_c^r$ , the corrected absolute  $r$ -band magnitude.  $M_c^r = m_c^r - 5 \log D[\text{Mpc}] + 25$ ;

Col. (20): Ft, the Freeman type (1 or 2) of the galaxy (Freeman 1970).

## 10. Optical TF Relation

Below, we apply “forward” linear regressions to the TF equation  $M_c^r = a\eta_c + b$  for 8 measures of optical linewidths, where  $\eta \equiv \log V_c - 2.5$ . We are now concerned specifically with finding the linewidth definition which yields the smallest TF scatter. The correct derivation of the forward TF slope and zero-point requires that magnitudes be corrected for selection bias (W94, W96). Here we limit ourselves to relative differences where the exact bias treatment is not important.

The complete CF sample includes regions of density enhancements near the Perseus-Pisces (PP) Supercluster that must be excluded to avoid any further bias of the TF scatter. In C92, we identified a region of Quiet Hubble Flow (QHF) away from the influence of the Local Supercluster which is nearly orthogonal to the main direction of flow between PP and the Great Attractor (cf. also Courteau *et al.* 1993). The Coma Supercluster and the Great Wall are included in the QHF but no large-scale velocity features are visible there. Indeed, the mean infall signal in the vicinity of the Great Wall and the measured shear across it are both consistent with zero (C92, Bernstein *et al.* 1994, Dell’Antonio, Geller, & Bothun 1996). A measurement of TF scatter in the QHF region will thus provide a lower limit to the real TF scatter. This is especially true since bias corrections are neglected here. Such corrections tend to amplify scatter estimates (W96). A similar QHF control region can be defined for MAT’s sample (Mathewson & Ford 1994). However, the infall pattern due to the Great Attractor is not as clearly delineated there as at PP and differences between TF relations in the Southern QHF and GA regions are hardly noticeable.

We use linear least-square fitting to compute values of the TF dispersion for the full sample of 304 CF galaxies and its subset of 127 QHF galaxies. Values for  $W_{15}$ ,  $W_{20}$ ,  $W_{25}$ ,  $W_{hist}$ ,  $W_{prob}$ , and  $V_{max}$  exist for all galaxies but  $V_{2.2}$ ,  $V_{iso}$ , and  $V_{opt}$  may be missing for small systems (cf. §6.1.2). Fig. 15 shows TF relations for 6 combinations of fully corrected magnitude and linewidths. The open circles show all CF galaxies; those filled are specific to the QHF region only. A similar exercise was done for the 958 MAT galaxies and a subset of 310 QHF galaxies. Fit coefficients for both samples are reported in Table 4 below. The fits for MAT are as above except that  $W_{15}$  and  $W_{20}$  were replaced by  $V_{rot}$ , the advocated linewidth by MAT for final TF analysis.  $V_{iso}$  linewidths

were not measured for MAT data. The TF plots for that sample (not shown here) are similar to those of CF (cf. W97).

Table 4  
TF fits

	ALL CF galaxies			CF QHF galaxies		
	$a(\pm)$	$b(\pm)$	$\sigma_{TF}(\text{mag})$	$a(\pm)$	$b(\pm)$	$\sigma_{TF}(\text{mag})$
$W_{15}$	-6.34(0.24)	-20.74(0.03)	0.52	-5.89(0.32)	-20.74(0.04)	0.41
$W_{20}$	-6.35(0.24)	-20.74(0.03)	0.51	-5.96(0.39)	-20.75(0.04)	0.39
$W_{hist}$	-5.77(0.22)	-20.72(0.03)	0.51	-5.40(0.28)	-20.74(0.04)	0.39
$W_{prob}$	-6.66(0.26)	-20.26(0.04)	0.53	-6.03(0.32)	-20.35(0.05)	0.40
$V_{max}$	-6.09(0.26)	-20.62(0.03)	0.55	-5.34(0.36)	-20.69(0.05)	0.46
$V_{2.2}$	-6.36(0.22)	-20.77(0.03)	0.46	-6.17(0.28)	-20.77(0.03)	0.34
$V_{iso}$	-6.47(0.25)	-20.70(0.03)	0.45	-6.02(0.31)	-20.69(0.04)	0.36
$V_{opt}$	-6.99(0.33)	-20.60(0.04)	0.46	-6.92(0.42)	-20.59(0.05)	0.34
	ALL MAT galaxies			MAT QHF galaxies		
$V_{rot}$	-6.91(0.11)	-21.37(0.02)	0.61	-6.52(0.15)	-21.43(0.03)	0.58
$W_{hist}$	-6.51(0.10)	-21.46(0.02)	0.57	-6.62(0.17)	-21.49(0.03)	0.55
$W_{prob}$	-6.83(0.12)	-21.13(0.02)	0.59	-6.95(0.20)	-21.15(0.03)	0.57
$V_{max}$	-6.68(0.13)	-21.34(0.02)	0.64	-6.92(0.20)	-21.36(0.03)	0.62
$V_{2.2}$	-6.64(0.13)	-21.50(0.02)	0.56	-7.14(0.19)	-21.52(0.03)	0.51
$V_{opt}$	-6.76(0.22)	-21.41(0.03)	0.59	-6.38(0.34)	-21.46(0.05)	0.53

Slopes are of order 6.0 for the CF sample which is somewhat shallower than those reported in W97, regardless of bias correction. This stems from slightly improved linewidths and magnitudes. The MAT data show larger TF scatter than reported in W97; this is due to our use of MAT’s original magnitudes for heuristic reasons (improved magnitudes were derived in W97).

Local infall motions clearly inflate the TF scatter in the full CF sample. Both CF and MAT QHF samples show a tighter dispersion at all linewidths; this is especially true for the CF sample. As seen in Fig. 15, the scatter in magnitudes is essentially constant at all absolute luminosities for resolved *model* velocities yet it does increase slightly at the fainter (smaller) end for *histogram* linewidths. The possibility of curvature in this sample has been discussed in W97 but effects are weak. Histogram linewidths may exhibit more of a curved trend than model linewidths but statistics are too poor to rule in favor of a quadratic transformation.

“Isophotal” linewidths,  $V_{2.2}$ ,  $V_{iso}$ , and  $V_{opt}$ , yield the smallest TF residuals. These also showed lowest internal scatter for the CF sample (§7), though repeatability does not necessarily ensure scatter tightness in these TF correlations. For example,  $W_{hist}$  and  $W_{20}$  repeat with quite different accuracy yet they yield rather similar TF solutions, with identical  $\sigma_{TF}$ ’s for the CF sample.  $V_{max}$  also fares very poorly. Its internal error is satisfactorily low, yet as a TF observable, it yields the

worst TF solution, for both samples. The most favorable definition of TF linewidth so far, as inferred from both the CF and MAT data sets, is that of  $V_{2.2}$ .

Similar tests were performed by R97 with 25 galaxies in the vicinity of Coma. Their “Weighted Mean Method: Outer Segments” is equivalent to our  $V_{box}$ , and both techniques yield comparably poor results (not shown in Table 4). Their PMM measure is also identical (by definition) to our  $W_{prob}$ , yet their result seems more optimistic than ours. Our investigation yields a moderate-to-poor TF scatter for  $W_{prob}$  while R97 rate it as their second best. R97’s best measure actually comes from a weighted mean of the velocity points in the range  $\sim 0.5 - 2r_{opt}$ . This is a surprising measure of rotation since it extends beyond the normal reach of most ORCs (cf. fig. 4). Thus we are unable to reproduce their result. R97 also showed that velocities measured at  $1.3r_{1/2}$  yields a poor RMS TF scatter. For an exponential disk, this is equal to  $V_{2.2}$ ! Our results appear to differ from R97’s in most respects (though error bars in R97’s  $\sigma_{TFs}$  are larger since their sample is ten times smaller than CF). R97 intentionally avoided model fitting and therefore comparison with the majority of our model linewidths cannot be made.

It should also be mentioned that our lowest value of TF scatter (0.34 mag) compares favorably with mean dispersions from large TF calibrations based on H I linewidths (G97).

## 11. Correlation with H I

As a final test for linewidth selection, we examine which of the tested measures of rotation best correlates with 21cm linewidths. A correlation between optical and radio velocity widths is expected on a dynamical basis. However, even well-developed ORCs rarely extend beyond  $1.5r_{opt}$  whereas H I RCs often reach as far as 3 to 5  $r_{opt}$  (Broeils 1992) (see Fig. 16).

Various calibrations of optical/radio linewidths have already been established. Thonnard (1983) found that 21cm linewidths measured at 50% of peak intensity yield a tight correlation:  $\langle V_{opt}^{max} - W_{21cm}^{50} \rangle = -1.5 \pm 3.9 \text{ km s}^{-1}$ . C92 compared line-of-sight rotational velocities for 205 CF galaxies with radio linewidths from the compilation of Giovanelli and Haynes (private communication 1990). A tight relationship was established with a slope of 1, minimal zero-point, and  $\sigma_{opt/21cm} = 24 \text{ km s}^{-1}$  (cf. C92, Fig. 5.9). In this correlation, the scatter was found to be remarkably constant over the full range of measured velocities ( $100 \leq V_{max} \leq 350 \text{ km s}^{-1}$ ). MAT showed the same trend and tight scatter from 75 to 290  $\text{km s}^{-1}$  for 219 galaxies (cf. their Fig. 5). Their best measured dispersion is  $\sigma_{opt/21cm} = 20 \text{ km s}^{-1}$ . A similar calibration by Vogt (1994) for 96 galaxies yields  $V_{opt} = 1.02W_{21cm} - 4 \text{ km s}^{-1}$  with  $\sigma_{opt-21cm} = 30 \text{ km s}^{-1}$ . From Table 1 of R97, we also compute  $V_{opt}^{PMM} = 0.95W_{21cm}^{50} - 5.76 \text{ km s}^{-1}$  ( $1\sigma = 13.41 \text{ km s}^{-1}$ ) and  $\Delta V_{opt}^{0.5-1r_{opt}} = 0.95W_{21cm}^{50} - 29.71 \text{ km s}^{-1}$  ( $1\sigma = 16.8 \text{ km s}^{-1}$ ). Although the canonical linewidth scatter is  $\sim 25\text{-}30 \text{ km s}^{-1}$ , the smaller values quoted by R97 stem mostly from the quixotical degree of pruning of their sample. Linewidths listed in their Table 1 do not include deprojection corrections, which also yield lower dispersion estimates.

To test our optical velocities against 21cm linewidths, we restrict our comparison to the recent list of Giovanelli, Haynes & coworkers (G97). This collection is the largest and most uniform compilation of published 21cm linewidths to date. Though G97 do include linewidths from various sources, we use only those directly measured by them. These widths are measured at 50% intensity of the profile horns.

Our comparisons use *fully corrected* linewidths to assess the maximum difference due to various transformations and sources of errors between final TF variables. We have derived the following linear and logarithmic transformations:  $V_c = AW_{GH} + B$  and  $\log V_c = A' \log W_{GH} + B'$ . Transformation coefficients are given in Table 5 below.

Table 5  
Optical/Radio Linewidth Transformations

	Linear Fit			Logarithmic Fit		
	$A(\pm)$	$B(\pm)$	$\sigma$	$A'(\pm)$	$B'(\pm)$	$\sigma'$
$W_{15}$	0.98(0.06)	-9.5(22.6)	41.6	0.969(0.080)	0.053(0.202)	0.063
$W_{20}$	0.98(0.06)	-10.0(22.1)	40.7	0.974(0.077)	0.040(0.195)	0.060
$W_{hist}$	1.10(0.07)	-42.7(24.6)	45.2	1.199(0.090)	-0.526(0.228)	0.070
$W_{prob}$	1.13(0.07)	0.8(25.8)	47.3	1.210(0.135)	0.068(0.197)	0.053
$V_{max}$	1.01(0.09)	-0.5(31.1)	57.2	0.990(0.128)	0.019(0.322)	0.099
$V_{2.2}$	0.99(0.05)	-0.1(17.0)	29.2	0.988(0.062)	0.019(0.155)	0.044
$V_{iso}$	1.00(0.06)	4.8(20.7)	33.6	1.003(0.074)	-0.006(0.183)	0.048
$V_{opt}$	0.99(0.08)	20.3(29.2)	39.1	0.892(0.107)	0.294(0.273)	0.047

Table 5: Fit coefficients for linewidth transformations from the system of G97. The standard deviations and zero-points of the fits are expressed in units of  $\text{km s}^{-1}$  or  $\log(\text{km s}^{-1})$ .

The optical rotational velocity which matches 21cm linewidths best, both in linear and log space, is again  $V_{2.2}$ . Its linear transformation slope is essentially one and the zero-point is consistent with zero, indicating a virtual one-to-one correspondence between  $V_{2.2}$  and the radio linewidth  $W_{21cm}^{50}$  of G97.  $V_{max}$  is again the worst contender. Our linear transformation for  $W_{hist}$  is also much poorer than that of Vogt (1994) who uses a similar algorithm. The zero-point offset is widely different and we find a larger dispersion (by  $10 \text{ km s}^{-1}$ ). The data from R97 also favor the PMM linewidth over a weighted-mean linewidth ( $\Delta V(0.5 - 1r_{opt})$ ) as a better match to radio linewidths, yet the latter yields a tighter TF scatter. No explanations for the trends seen by Vogt and R97 are offered at present. We contend for now that our *model* linewidths  $V_{2.2}$  and  $V_{iso}$  provide the closest match to the H I linewidths of G97.

The tight and constant scatter at all luminosities between (suitably chosen) optical/radio linewidths (C92, MAT, Vogt 1994) may appear surprising given that resolved H I RCs extend far beyond the optical radius. Fig. 16 shows series of re-scaled H I RCs from Broeils (1992) to illustrate this point. The arrow indicates the location of the optical radius. As seen in panels b)



and c) (most appropriate for comparison with typical TF galaxies), many H I RCs keep rising beyond  $r_{opt}$ . Perusal of Appendix A (see also MAT, Rubin *et al.* 1989) also shows many ORCs which have not reached any turnover by the last point of detection (see also Fig. 14). It is often assumed that optical linewidths should be biased *low* in comparison to radio data, especially in low mass systems. However, unlike resolved H I RCs, H I linewidths *do not* sample outer disks effectively since the H I surface density drops rapidly beyond the optical radius (Cayatte *et al.* 1994, Broeils & van Woerden 1994, Broeils & Rhee 1997). The amount of H I inside  $r_{opt}$  is typically greater than 50 – 60% of the total. This holds true for the majority of spiral types (Cayatte *et al.* 1994, Roberts & Haynes 1994). H I linewidths are thus weighted heavily by the H I flux inside the optical radius. Hence, it is not surprising that optical resolved velocity widths and H I integrated linewidths should match so well. For low and intermediate mass galaxies (Fig. 16a,b), the H I profile width may therefore be less than twice the true maximum velocity.

Modelling the interplay between the shape of the rotation curve, the H I surface density, and the width of the global H I profile is an important task. The correlation between 21cm linewidths and the true maximum rotational velocity of spiral galaxies, often assumed to be unity but surely smaller, would be of great benefit for dynamical studies. Exploratory investigations are being conducted (*e.g.* Schulman *et al.* 1997) but a clear picture is still lacking.

A significant fraction (30%) of disk galaxies also reach their peak velocity close to the optical radius which reinforces the tight optical/radio linewidth correlation. Fig. 17 shows the distributions of peak rotational velocities from the (resolved) optical and H I RCs of CF and Broeils (1992) respectively. The open circles represent only those galaxies in CF that have achieved convergence (§6.3) and Broeils’ galaxies are shown as filled circles labelled with their catalog name. The solid line represents a transition between HSB and dwarf galaxies. Above that line, most of the galaxies show a turnover near  $4 - 5h$  which is just within the limits of optical detection by conventional long-slit spectrographs.

## 12. Summary

We have presented a new collection of optical RCs for 304 late-type spirals, here referred to as the Courteau-Faber (CF) sample. The first sections of this paper discussed data reduction procedures and extraction of RCs from resolved H $\alpha$  spectra. Our rotation curves were shown to be in excellent agreement with similar data taken by different authors with different telescopes (Amram, Mathewson, Rubin, and Vogt). An empirical function was adopted to model the shape, amplitude, and zero-point (radial velocity) of each ORC, and then used to infer stable linewidths for TF applications. An additional fitting parameter was sometimes included to account for rising or declining RCs beyond the optical radius. Strong covariances are unavoidable in this multi-parameter modelling. A two-parameter prescription, like the arctan function, is required to minimize internal coupling between the fitted parameters. We also modelled 958 RCs from the collection of Mathewson *et al.* (1992) using the same fitting functions.

We pointed out that the “Universal Rotation Curve” of Persic, Salucci, & Stel (1996) is not a perfect tracer of fast rising bulges and declining outer disks. This shortfall of the model may soon be remedied by accounting at least for a bulge component (Salucci 1997, private communication). Because of matching uncertainties at large radii, use of the URC model is not recommended to extrapolate isophotal TF linewidths. The model-dependency of the URC via  $r_{opt}$  and metric requirement to define  $L_B$  are additional sources of ambivalence.

The latter half of this paper focused on determining the best measure of rotational velocity for TF work. Our selection was based on three criteria:

- Smallest internal scatter (*i.e.* robust to observational errors),
- Minimal TF residuals, and
- Best match to radio (21cm) linewidths.

The best linewidths are those determined via multi-parameter fitting. Modelling smooths out all effects of non-circular motions which are particularly acute in long-slit data. Internal repeatability is thus maximized. The best measure of TF velocity is  $V_{2.2}$ , the location of peak rotational velocity for a pure exponential disk.  $V_{2.2}$  is interpolated from the *model* rotation curve at  $r_{disk}(= 2.15h$ , where  $h$  is the disk exponential scalelength.) This definition ranked with the best in all three categories above. The distinction of yielding smallest residuals in TF diagrams is shared by essentially any *isophotal* linewidths (here,  $V_{iso}$  and  $V_{opt}$ ).

It is possible to define an optical rotational velocity for TF use which is an identical match to radio linewidths. We showed that  $V_{2.2}$  provides such a match for  $W_{21cm}^{50}$ , the radio linewidth measured at 50% of peak intensity by G97. The good agreement between optical and radio linewidths is understood because a large fraction (50-60%) of the H I surface density is actually contained within the optical radius, and, in addition, a significant fraction (30%) of ORCs also reach their peak velocity before  $r_{opt}$ .

Finally, TF calibrations based solely on optical linewidths can yield as robust and accurate measures of TF distances as analyses based on H I linewidths, provided the choice of optical linewidth is made judiciously.

Tables 3, 6, and 7, together with the figures in Appendix A will be fully released in the AAS CD-ROM Series (vol. 8).

## Acknowledgements

I would like to thank Michael Strauss for a thorough reading of an early draft and many valuable suggestions. Many thanks as well to Adrick Broeils for permission to use data from his thesis (Fig. 16) and useful discussions on H I linewidths and turbulence corrections. Hans-Walter Rix offered pertinent comments, especially on §5, and Gary Bernstein clarified some issues regarding  $W_{prob}$ .

I would like to express my gratitude to Jesús González, former officemate and graduate student at UC Santa Cruz, for patient introductions to the art of long-slit reductions. Sandra Faber oversaw production of this work at its early stage; she is thanked warmly for all her support.

Vera Rubin kindly supplied paper tracings of ORCs from photographic plates (§4) and Alan Dressler also took beautiful data for us at Las Campanas Observatory in 1990.

Much of the data collection and reductions was carried out while the author was in graduate school. Financial support was provided by Canadian NSERC and FCAR graduate fellowships as well as by Sandra Faber's NSF grant AST 87-02899.

## Appendix A. RCs and Models

H $\alpha$  RCs are presented for 304 Sb-Sc galaxies in the CF sample. These are shown on the plane of the sky. Multiple observations are not overlapped but shown separately to avoid crowding. A total of 376 separate RCs are presented. For each galaxy, two plots are shown with the full two-sided and one-sided curves on the left and right panels respectively. The label above the left window for each galaxy shows its name and observing date. The bottom axis of the right window is given in units of arcseconds and the top is in kpc ( $H_0 = 70 \text{ km s}^{-1} \text{ Mpc}^{-1}$ ). Error bars have also been omitted to avoid crowding; their amplitudes out to the last saved point match roughly the size of the data circles.

The center of each RC, about which to fold the curve, was determined from Model 2 fits. On the right panels (for folded RCs), open circles with a dash at the center represent approaching velocities ( $v < 0$ ) while those with a cross denote receding velocities ( $v > 0$ ). The vertical dotted line in the right panels is plotted at  $r_{disk}$  ( $=2.15h$ ), the radius of peak rotational velocity for a pure exponential disk. This line is only shown if photometry is available in Paper I.

Models 1 and 2 (see §5) are shown by a long-dash line and a continuous line respectively. The URC parameterization of PSS is represented with a dotted curve. The latter could not be plotted if  $L_B$  was not listed in the RC3 or if  $r_{opt}$  was not available.

The full content of Appendix A includes 55 pages of figures. Only the first page is presented here. The full series will be released in the AAS CD-ROM Series (vol. 8).

## Appendix B. Model Parameters

Fit parameters for Models 1 and 2 are presented for all 304 CF galaxies and 958 MAT galaxies. These are given in Tables 6 and 7 respectively. A number of MAT RCs included in the compilation of Persic & Salucci (1995; hereafter PS) were not fitted due to poor signal-to-noise or impossibility to define a rotation center. Those are: 140-g23, 375-g60, 382-g32, 416-g28, 418-g9, 540-g10, and 565-g23.

The center values ( $v_0$  and  $r_0$ ) from Model 1 and 2 for each MAT galaxy were virtually identical. For convenience, the centers from Model 2 only were shown in Table 7. As before, the full content of these tables will be released in computer-readable files in the AAS CD-ROM Series.

Our re-derivation of the recession velocity for MAT galaxies can be compared with that of PS. This comparison is shown in Fig. 18 where we plot the difference between our measured  $v_0$  and the value determined by PS. Each galaxy is represented by its ESO/LV catalog name. The scatter is appreciably larger than what we get by comparing our solutions between Model 1 and 2, as well as other fitting techniques (we also explored spline fits to the RC to determine its center). Different weighting schemes could explain the discrepancy.

### Appendix C. Intensity-Weighted Centroids

To determine the error in the position of the centroids using intensity weighting, define  $x_i$  and  $f_i$  as the position and intensity at each pixel  $i$ . The centroiding algorithm used a total of 5 pixels centered about the intensity peak,  $x_0$ , of the emission feature at each row. The emission-line centroid is given by:

$$\langle x \rangle = \frac{\sum_i (x_i - x_0) f_i}{\sum_i f_i} = \sum_i (x_i - x_0) w_i \quad (1)$$

where we have defined the pixel weights

$$w_i \equiv \frac{f_i}{\sum_i f_i} = \frac{f_i}{F}, \quad (2)$$

and where  $F$  is the total flux under the curve. The error of the centroid is given by

$$\sigma^2 \langle x \rangle = \sum_i (x_i - x_0)^2 \sigma_{w_i}^2 + \sum_{i,j} (x_i - x_0)(x_j - x_0) \sigma_{w_i w_j}. \quad (3)$$

Note that the pixels are oversampled (by a factor two or three) due to seeing, is not correlated since they are sampled independently. Therefore, the covariance term in eq. (4) vanishes and we can write,

$$\sigma^2 \langle x \rangle = \sum_i (x_i - x_0)^2 \left\{ \frac{\sigma_{f_i}^2}{f_i^2} + \frac{\sigma_F^2}{F^2} \right\} w_i^2 \quad (4)$$

where  $\sigma_F^2 = \sum \sigma_{f_i}^2$ . Both terms  $\sigma_{f_i}^2$  and  $\sigma_F^2$  come from photon statistics and are measured from the variance image. The first term inside brackets can be interpreted as the fractional error in the intensity at each pixel. The second term gives the signal-to-noise ratio of the total intensity of the line, *i.e.* ,

$$S/N = \frac{F}{\sigma_F}. \quad (5)$$

The method of Gaussian fitting yields similar values for the line centers (within 0.1 pixels) at  $S/N > 20$  but is not as robust as intensity-weighted centroids in conditions of low  $S/N$ . In an attempt to increase the  $S/N$ , we also tested “triple-Gaussian” fits - those which include the lines of  $\text{H}\alpha$  and  $[\text{N II}]$  simultaneously, but did not achieve appreciable gains. It should be noted that the error term given in Eq. 4 is  $\sim 10\%$  smaller than the value obtained via Gaussian fitting.

The fitting of emission centroids at each row uses a technique of parabolic-binned interpolation. CCD pixel values are an integral of the product of the spectrum and the pixel response function. In bin interpolation, it is the integral of the interpolating function rather than the function itself that is constrained to match the pixel values. A parabolic-binned interpolation fits a parabola whose area within each pixel (rather than its value at the center of the pixel) matches the pixel values.

Consider a series of CCD pixel values (see Fig. 19) fitted with the parabola

$$y(x) = a_0 + a_1x + a_2x^2$$

The position of the function maximum ( $dy = 0$ ) is given by

$$x_{max} = \frac{-a_1}{2a_2} \quad \text{and} \quad y_{max} = a_0 - \frac{1}{4} \frac{a_1^2}{a_2}$$

Let us use for simplicity  $x_0 = 0$ ,  $x_- = -1$ , and  $x_+ = +1$ . A standard parabolic fit through each point yields,

$$\left. \begin{aligned} y_0(x_0) &= a_0 \\ y_-(x_-) &= a_0 - a_1 + a_2 \\ y_+(x_+) &= a_0 + a_1 + a_2 \end{aligned} \right\} \begin{aligned} a_0 &= y_0 \\ a_1 &= (y_+ - y_-)/2 \\ a_2 &= (y_+ + y_-)/2 - y_0 \end{aligned}$$

However, taking the binned nature of the data into account, we must integrate the area at all pixels, that is

$$\begin{aligned} y_0 &= \int_{-1/2}^{1/2} y(x)dx = a_0 + \frac{a_2}{12} \\ y_- &= \int_{-3/2}^{-1/2} y(x)dx = a_0 - a_1 + \frac{13}{12}a_2 \\ y_+ &= \int_{1/2}^{3/2} y(x)dx = a_0 + a_1 + \frac{13}{12}a_2 \end{aligned}$$

Inverting the transformation gives,

$$\bar{\mathbf{a}} = \begin{pmatrix} a_0 \\ a_1 \\ a_2 \end{pmatrix} = \begin{pmatrix} 13/12y_0 - (y_+ + y_-)/24 \\ (y_+ - y_-)/2 \\ (y_+ + y_-)/2 - y_0 \end{pmatrix}$$

Comparison of this solution for a parabolic-binned interpolation and the basic parabolic fit at the pixel centers above shows an offset for the terms  $a_0$ . The two differ by

$$\frac{1}{12} \left( y_0 - \frac{y_+ + y_-}{2} \right).$$

Our measurements properly account for this difference.

## REFERENCES

- Aaronson, M., *et al.* 1989, ApJ, 338, 654
- Amram, P. *et al.* 1992, A&A, 263, 69
- Amram, P. *et al.* 1994, A&AS, 263, 69
- Ashman, K.M. 1990, ApJ, 359, 15
- Balkowski, C., Bottinelli, L., Chamaraux, P., Gouguenheim, L., Heidmann, J. 1974, A&A, 34, 43
- Bershady, M.A., 1995, in “Galaxies in the Young Universe,” eds. H. Hippelein, K. Meisenheimer, & H-J. Roser, (Springer:Berlin), 139
- Bershady, M.A., 1997, in “Dark and Visible Matter in Galaxies and Cosmological Implications,” eds. M. Persic & P. Salucci (ASPCS), 537
- Bernstein, G.M., Guhathakurta, P., Raychaudhury, S., Giovanelli, R., Haynes, M.P., Herter, T., & Vogt, N.P., 1994, AJ, 107, 1962
- Bicay, M.D. & Giovanelli, R. 1986, AJ, 91, 705.
- Blumenthal, G.R., Faber, S.M., Primack, J.R., & Rees, M.J. 1984, Nature, 311, 517.
- Bosma, A., Byun, Y., Freeman, K.C., Athanassoula, E., 1992, ApJ, 400, 21
- Bothun, G. D., Aaronson, M., Schommer, R. A., Mould, J. R., Huchra, J. P., & Sullivan, W. T. 1985, ApJS, 57, 423
- Bothun, G. D., & Mould, J. R. 1987, ApJ, 313, 629
- Bottinelli, L., Gouguenheim, L., Paturel, G., & de Vaucouleurs, G., 1983, A&A, 118, 4
- Bottinelli, L., Gouguenheim, L., Paturel, G., & de Vaucouleurs, G., 1984, ApJ, 280, 34
- Bottinelli, L., Chamaraux, P., Gerard, E., Gouguenheim, L., Heidman, J., Kases, I., & Lauque, R. 1971, A&A, 12, 264.
- Brandt, J., 1960, ApJ, 131, 293
- Broeils, A.H. 1992, Ph.D. thesis, Univ. Groningen
- Broeils, A.H. & Courteau, S. 1997, in “Dark and Visible Matter in Galaxies and Cosmological Implications,” eds. M. Persic & P. Salucci (ASPCS), 74
- Broeils, A.H. & van Woerden, H. 1994, A&A, 107, 129
- Broeils, A.H. & Courteau, S. 1998, in preparation
- Burstein, D., Willick, J. A., & Courteau, S. 1995, in The Opacity of Spiral Disks, ed. J.I. Davies & D. Burstein (Nato Series; Kluwer:Dordrecht), 73



- Cayatte, V., Kotanyi, C., Balkowski, C., & van Gorkom, J.H 1994, *AJ*, 107, 1003
- Cole, S., Aragón-Salamaca A., Frenk, C.S., Navarro, J.F., & Zepf, S.E. 1994, *MNRAS*, 271, 781
- Courteau, S. 1992, Ph.D. thesis, Univ. California, Santa Cruz (C92)
- Courteau, S. 1996, *ApJS*, 103, 363 (C96, Paper I)
- Courteau, S. and Faber, S.M. 1988, in “The Extragalactic Distance Scale”, eds. S. van den Bergh and C. Pritchet (ASPCF), 366
- Courteau, S., de Jong, R., & Broeils, A.H. 1996, *ApJ*, 457, L73
- Courteau, S., Faber, S.M., Dressler, A., & Willick, J.A. 1993, *ApJ*, 412, L51
- Courteau, S. & Rix, H.-W. 1997, submitted, astro-ph 97...
- Courteau, S., Sohn, Y.-J., & Faber, S.M. 1997, in preparation
- Dell’Antonio, I.P., Geller, M.J., Bothun, G.D. 1996, *AJ*, 112, 1780
- Dressler, A., & Faber, S.M. 1990, *ApJ*, 354, 45.
- Eisenstein, D.J., 1996, Ph.D. thesis, Princeton University
- Eisenstein, D.J., & Loeb, A. 1996, *ApJ*, 459, 432
- Faber, S.M. 1982, *Astrophysical Cosmology*, eds H. Brück, Coyne, G.V., & Longair, M.S. (Pontifical Scientific Academy, Vatican), 191
- Fall, S.M., & Efstathiou, G., 1980, *MNRAS*, 193, 189.
- Flores, R., Primack, J.R., Blumenthal, G.R., & Faber, S.M. 1993, 412, 443
- Franx, M., & de Zeeuw, T. 1992, *ApJ*, 392, 47
- Freeman, K. C. 1970, *ApJ*, 160, 811
- Freudling, W. 1990, Ph.D. thesis, NAIC/Cornell Univ.
- Gilmore, G.F., King, I.R., van der Kruit, P.C. 1990, *The Milky Way As A Galaxy*, eds. R. Buser & I.R. King (University Science Books, California), 212
- Giovanelli, R. *et al.* 1997, *AJ*, 113, 53 (G97)
- Giovanelli, R. *et al.* 1997, *AJ*, 113, 22
- Giovanelli, R. *et al.* 1994, *AJ*, 107, 2036
- Giraud, E.H. 1986, *A&A*, 164, 17
- González, J.J. 1993, Ph.D. thesis, Univ. California, Santa Cruz

- Gunn, J.E. 1982, *Astrophysical Cosmology*, eds H. Brück, Coyne, G.V., & Longair, M.S. (Pontifical Scientific Academy, Vatican), 233
- Han, M.S. 1991, Ph.D. thesis, California Inst. Technol.
- Haynes, M.P., *et al.* 1997, AJ, 113, 1197
- Haynes, M.P., & Giovanelli, R. 1984, AJ, 89, 758
- Kauffman, G., *etal* 1993, MNRAS, 264,201.
- Kogut, A., *et al.* 1993, ApJ, 419, 1
- Kravtsov, A.V., Klypin, A.A., Bullock, J.S., & Primack, J.R. 1997, astro-ph/9708176
- Lauberts, A. 1982, The ESO/Uppsala Survey of the ESO (B) Atlas (Garching: ESO)
- Lauer, T.R., & Postman, M. 1994, ApJ, 425, 418
- Lauer, T.R., Stover, R.J., & Terndrup, D. 1983, *The VISTA Users Guide*, Lick Obs. Tech. Rep. 34
- Loveday, J., Peterson, B.A., Efstathiou, G., & Maddox, S.J. 1992, ApJ, 390, 338
- Malhotra, S., Spergel, D.N., Rhoads, J.E. & J. Li 1997, ApJ, 473, 687
- Marzke, R.O., da Costa, L.N., Willmer, C., & Pellegrini, P.S., preprint
- Mathewson, D. S. & Ford, V. L., 1994, ApJ, 434, L39
- Mathewson, D. S., Ford, V. L., & Buchhorn, M. 1992, ApJS, 81, 413 (MAT)
- Miller, J.S. & Stone, R.P.S. 1987, *The CCD Cassegrain Spectrograph at the Shane Reflector*, Lick Observatory Technical Reports No. 48
- Miller, J.S. & Stone, R.P.S. 1993, *The Kast Double Spectrograph*, Lick Observatory Technical Reports No. 66
- Mould, J. R., Akeson, R. L., Bothun, G. D., Han, M. S., Huchra, J. P., Roth, J., & Schommer, R. A. 1993, ApJ, 409, 14 (HM)
- Navarro, J.F. 1997, in “Dark and Visible Matter in Galaxies and Cosmological Implications”, eds. M. Persic & P. Salucci, (ASPCS), 404
- Navarro, J.F., Frenk, C.S., & White, S.D.M. 1996, ApJ, 462, 563
- Oepik, E. 1922, ApJ, 55, 406
- Osterbrock, D. E., & Martel, A. 1992, PASP, 104, 76
- Peletier, R. F., & Willner, S. P. 1991, ApJ, 382, 315
- Peletier, R. F., & Willner, S. P. 1993, ApJ, 418, 626

- Persic, M., Salucci, P., & Stel, F. 1996, MNRAS, 281, 27 (PSS)
- Persic, M., & Salucci, P., 1995, ApJS, 99, 501
- Pierce, M. J., & Tully, R. B. 1988, ApJ, 330, 579
- Pierce, M. J., & Tully, R. B. 1992, ApJ, 387, 47
- Raychaudhuri, S., von Braun, K., Bernstein, G. M., & Guhathakurta, P. 1997, AJ, 113, 2046 (R97)
- Regan, M.W., & Vogel, S.N. 1994, ApJ, 434, 536
- Rhee, M.-H. 1992, Ph.D. thesis, Univ. Groningen
- Rhee, M.-H. & Broeils, A.H. 1997, A&A, submitted
- Rhoads, J.E. 1997, AJ, to be published in xxx issue.
- Rix, H-W., Guhathakurta, P., Colless, M., & Ing, K. 1997, MNRAS, 285, 779
- Roberts, M.S. 1978, AJ, 83, 1026
- Roberts, M.S., & Haynes, M.P. 1994, ARA&A, 32, 115
- Rood, H.J. & Williams, B.A. 1993, MNRAS, 263, 211
- Rubin, V. C., 1995, ApJ, 451, 419
- Rubin, V. C., & Ford, W. K., 1986, ApJ, 305, 35
- Rubin, V. C., Ford, W. K., & Thonnard, N. 1980, ApJ, 238, 471
- Rubin, V. C., Kenney, J. D., Boss, A. P., & Ford, W. K. 1989, AJ, 98, 1246
- Rubin, V. C., Burstein, D., Ford, W. K., & Thonnard, N. 1985, ApJ, 289, 81
- Schlegel, D.J. 1995, Ph.D. thesis, Univ. California, Berkeley
- Schommer, R.A., Bothun, G.D., Williams, T.B., & Mould, J.R. 1993, AJ, 105, 1993
- Schulman, E., Brinks, E., Bregman, J.N., & Roberts, M.S. 1997, AJ, 113, 1559
- Shostak, G.S. 1975, ApJ, 198, 527
- Silk, J. 1995, in The Opacity of Spiral Disks, ed. J.I. Davies & D. Burstein (Nato Series; Kluwer:Dordrecht),
- Silk, J. 1997, ApJ, 481, 703
- Sofue, Y. 1997, PASJ, 49, 17
- Storchi-Bergmann, T. 1991, MNRAS, 249, 404

- Strauss, M. A., & Willick, J. A. 1995, *Phys. Rep.*, 261, 271
- Thonnard, N. 1983, in *Internal Kinematics and Dynamics of Galaxies*, ed. E. Athanassoula, (Dordrecht: Kluwer), p.29.
- Tully, R.B., & Fisher, J.R. 1977, *A&A*, 54, 661
- Tully, R.B., & Fouqué, P. 1985, *ApJS*, 58, 67
- van Driel, W., van den Broek, A.C., & Baan, W.A. 1995, *ApJ*, 444, 80
- Vogt, N.P. 1994, PhD thesis, Cornell University
- Vogt, N. P., Herter, T., Haynes, M. P., & Courteau, S. 1993, *ApJ*, 415, L95
- Vogt, N. P., Forbes, D.A., Phillips, A.C., Gronwall, C., Faber, S.M., Illingworth, G.D., & Koo, D.C. 1997, *ApJ*, 465, L15
- White, S.D.M., 1991, in *The Dynamics of Galaxies and Their Molecular Cloud Distribution*, eds. F. Combes & F. Casoli, (Dordrecht: Kluwer), p. 383
- Willick, J. A. 1991, Ph.D. thesis, Univ. California, Berkeley (W91)
- Willick, J. A. 1994, *ApJS*, 92, 1
- Willick, J. A., Courteau, S., Faber, S. M., Burstein, D., & Dekel, A., 1995, *ApJ*, 446, 12
- Willick, J. A., Courteau, S., Faber, S. M., Burstein, D., Dekel, A., & Kolatt, T. 1996 *ApJ*, 457, 460 (W96)
- Willick, J. A., Courteau, S., Faber, S.M., Burstein, D., Dekel, A., & Strauss, M. A. 1997, *ApJS*, 109, 333 (W97)

Fig. 1.— Example of a raw spectrum corrected for geometrical distortion. The galaxy is UGC 1437. This figure should be compared with Rubin’s photographic spectrum for the same galaxy (NGC 753) shown in Rubin *et al.* (1980, Plate 17). The depth of exposure is comparable (see also Fig. 5, top left panel).

Fig. 2.— Same spectrum as Fig. 1 but with the skylines removed.

Fig. 3.— Spectrum of UGC 1437 with the skylines *and* continuum removed. The image is now ready for extraction of the rotation curve. Note that the lines [S II] are barely visible. The continuum subtraction is accurate over most of the chip except for deviations of a percent or so at the position of absorption lines or where night sky lines and continuum once intersected, as well as long-ward of 6800 Å where focus variations become significant.

Fig. 4.— Histogram of the maximal extent of ORCs for our sample.  $r_{max}$  is taken to be the largest radius of detection on either the approaching or receding side. The disk exponential scalelength  $h$  is measured from 1D bulge-to-disk decompositions (Paper I, Broeils & Courteau 1997). The fall-off beyond the optical radius at  $3.2h$  is due to the rapid decline in H $\alpha$  flux density.

Fig. 5.— Comparisons with the RCs from Rubin and coworkers. The latter are represented by large open squares and ours with smaller filled circles (and open circles, filled squares, or open triangles for duplicate observations of our own.) Some eye-ball smoothing was applied by Rubin; our data are shown as sampled by the detector (no spatial binning). No corrections were applied for inclination or redshift broadening.

Fig. 6.— Comparisons with the RCs MAT. MAT’s data are represented by open squares and ours with filled circles. MAT’s data were binned (smoothed) on a  $2''$  scale.

Fig. 7.— a) Comparisons with the RCs of Vogt (1994). The point types follow the same convention as in Fig. 5 and 6. The systemic velocities for Vogt’s U8488 and U11809 curves were readjusted to better match our RCs.

Fig. 7.— b) Comparisons with the RCs of Vogt (1994).

Fig. 8.— Comparisons with the Fabry-Perot RCs of Amram *et al.* (1992, 1994).

Fig. 9.— Example of arctan models for the fitting of resolved RCs. Different values of the truncation radius,  $r_t$ , are shown for six models with  $v_c = 200 \text{ km s}^{-1}$ . Note that  $r_t$  is not strictly equal to the radius at turnover.

Fig. 10.— Example of the multi-parameter fitting function for resolved ORCs. Different values of the shape parameter  $\gamma$  are shown for six models with  $v_c = 200 \text{ km s}^{-1}$  and  $r_t = 10$ . For a high-enough  $\gamma$ ,  $r_t$  does correspond to the exact location of the RC turnover. Variations with the  $\beta$  parameter, though seldom used, are also shown as dotted lines.

Fig. 11.—  $\chi^2$  differences between Model 2 and Model 1 fits for CF and MAT galaxies. A preponderance of negative differences favors the best fitting function. The fit parameters  $r_t$  and  $\gamma$  are from Model 2.

Fig. 12.— Distribution of  $r_t/r_{opt}$  against  $\gamma$  for Model 2 with CF galaxies. The parameter coupling is strong for  $r_t/r_{opt} \leq .3$  and  $\gamma \leq 2.5$ . This explains the “hook” at small  $\gamma$ ’s observed in the right panels of Fig. 11. The filled circles show the brighter half of the CF sample and the open squares represent the fainter half.

Fig. 13.— Flux-weighted integrated profile for UGC1437. The various flux levels which define our measures of rotational linewidths are described in the text. The vertical arrows show the profile boundaries inside of which a total area is computed. The fractional intensity levels are determined via parabolic-binned interpolation (Appendix C).

Fig. 14.— Histogram of logslopes from data ( $ls_r$ ) and Model 2 ( $ls_m$ ). RCs with  $ls \leq 0.2$  are deemed convergent. 60% of all the CF galaxies satisfy that criterion.

Fig. 15.— TF calibrations for six definitions of linewidths (described in the text.) Open circles correspond to all CF galaxies. Filled circles represent “Quiet Hubble Flow” galaxies which are less perturbed by streaming and local infall motions. Linewidths are fully corrected, as explained in the text.

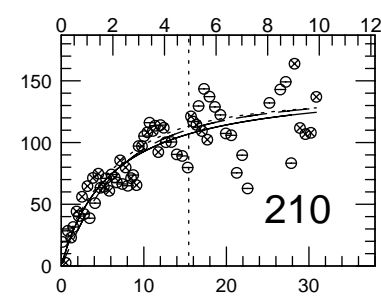
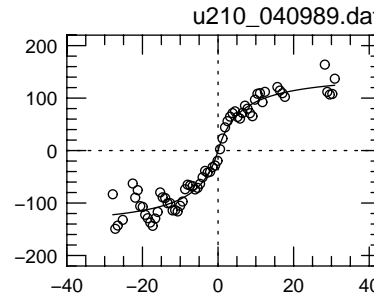
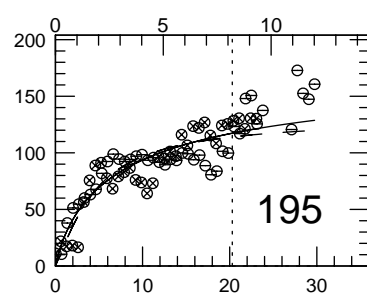
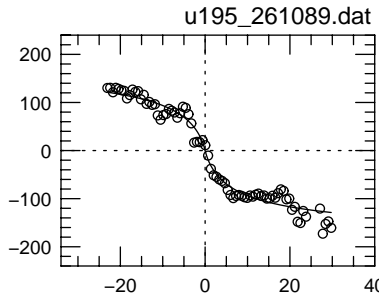
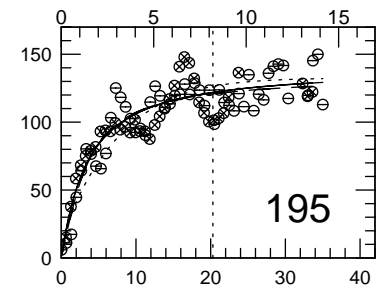
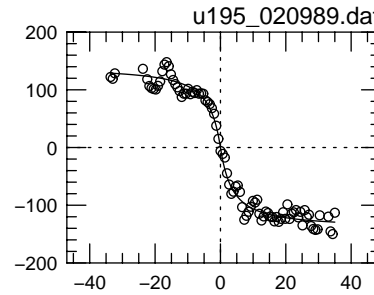
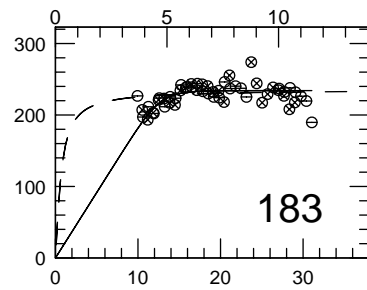
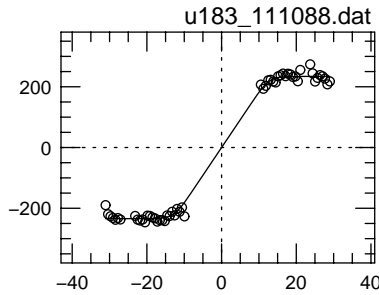
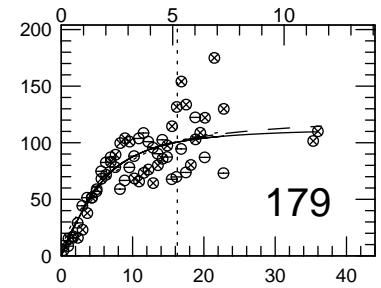
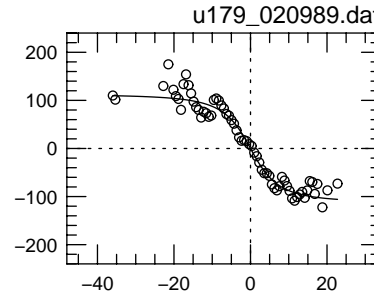
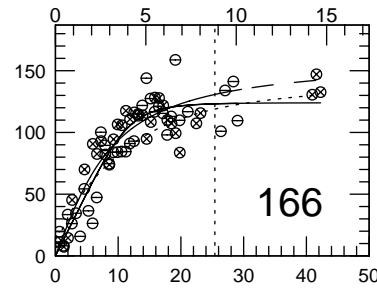
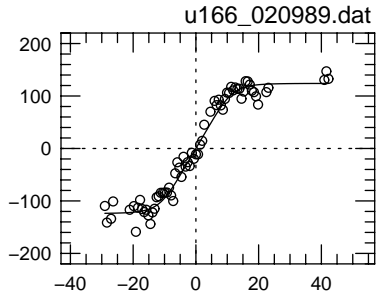
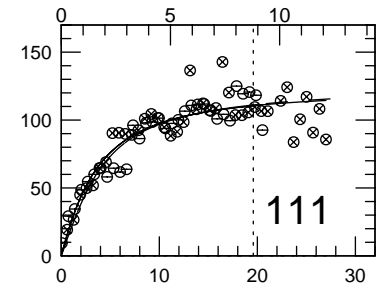
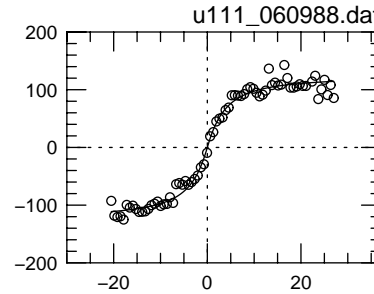
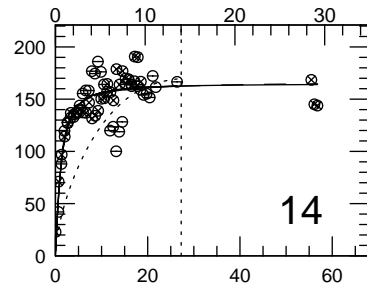
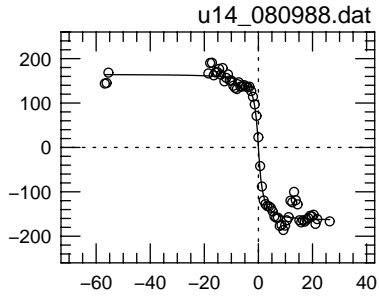
Fig. 16.— Resolved RCs from H I maps of nearby galaxies (figure adapted with permission from Broeils (1992).) The radius is normalized by the disk exponential scalelength  $h$ . The vertical arrow in each panel indicates the location of the optical radius ( $r_{opt} \sim 3.2h$ ). Most of the intermediate and bright galaxies show a velocity peak before or near  $r_{opt}$ .

Fig. 17.— Comparison of (twice) the maximum rotational speed against the ratio of  $r_{peak}$ , the radius at maximum velocity, normalized by the disk scalelength. The open circles data come from CF ORCs (Model 2) which satisfy  $ls_m \leq 0.2$  and the filled circles are measured from extended H I RCs from the compilation of Broeils (1992). The horizontal line at  $240 \text{ km s}^{-1}$  is a broad demarcation between “TF”, fast (HSB galaxies) and slower (LSB and dwarf galaxies) rotators. This figure confirms the matching trends between radio and ORCs for large galaxies within 4-5 scalelengths. The dotted vertical line shows the location of  $r_{opt}$ . The inset shows the histogram for all CF galaxies in this figure. Radio and optical RCs are shown to peak at roughly the same location near the optical radius. This supports the good correlation between radio and ORC linewidths for bright galaxies (§11).

Fig. 18.— Difference in systematic velocities between CF (Model 2) and the models by Persic & Salucci (1995) for 958 MAT galaxies. The points are labelled by their galaxy name.

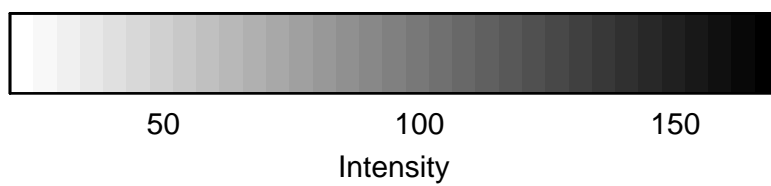
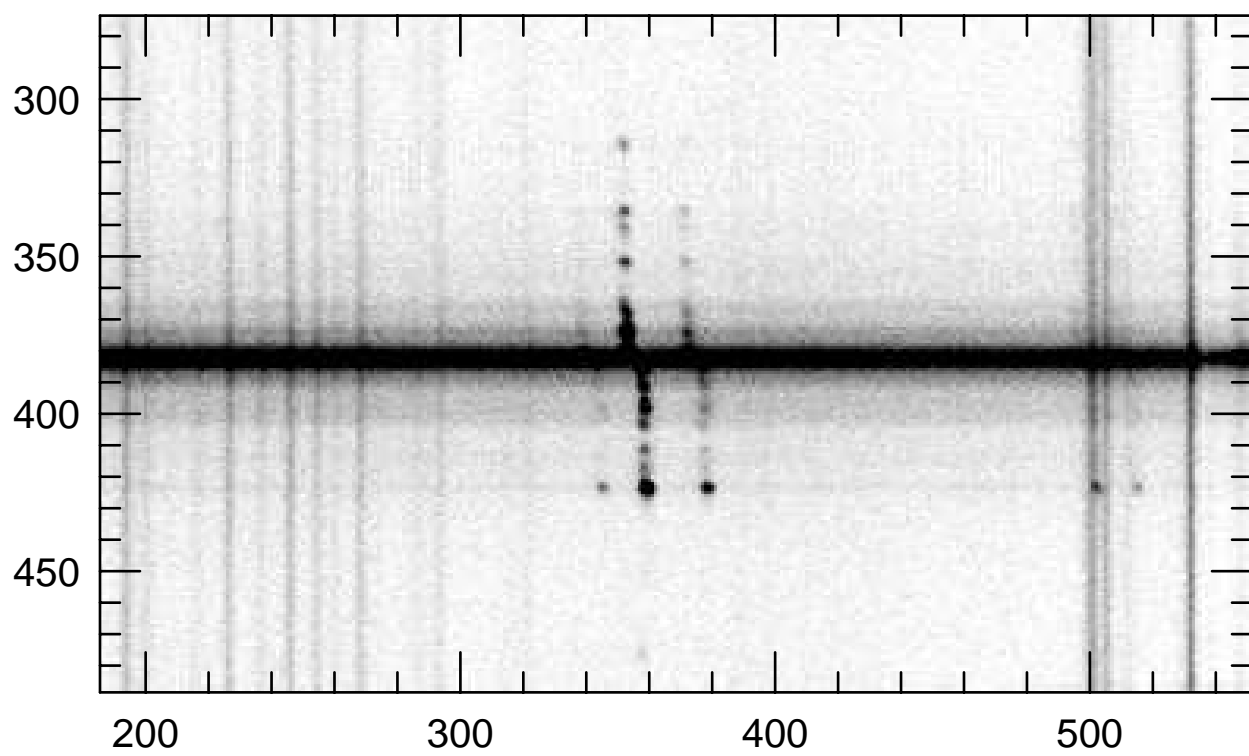
Fig. 19.— Illustration of parabolic-binned interpolation. The pixels centroids are determined by integration of the area at all pixels. This technique yields accurate sub-pixel interpolations to estimate fractional flux levels from binned data.

Line-of-Sight Velocity (km s<sup>-1</sup>)

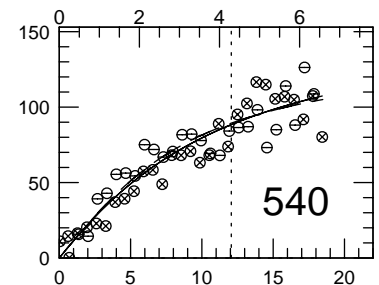
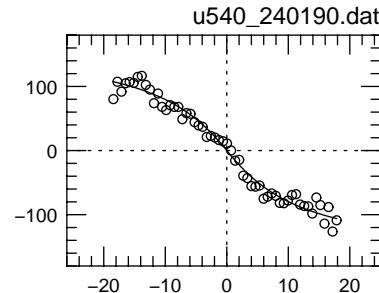
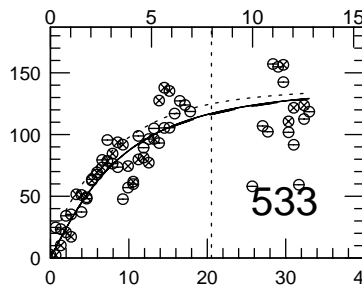
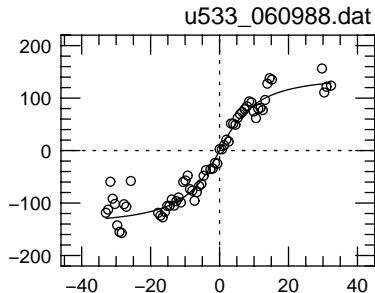
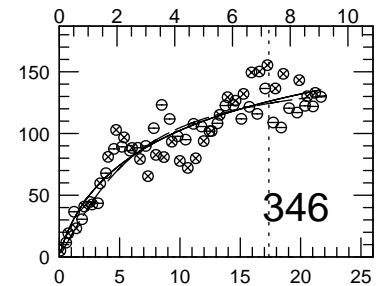
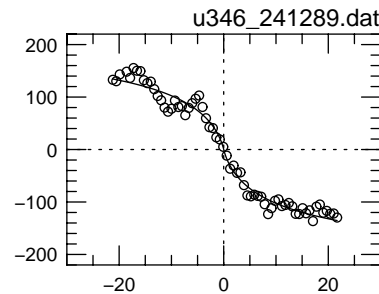
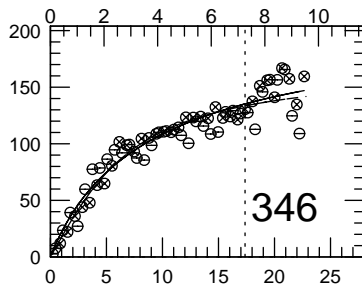
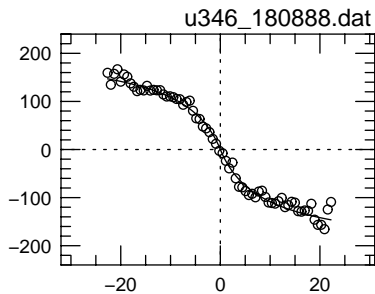
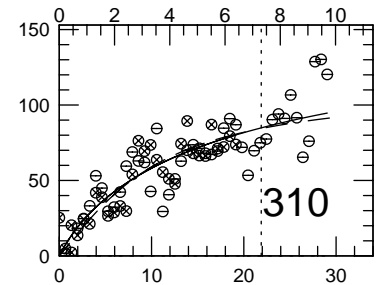
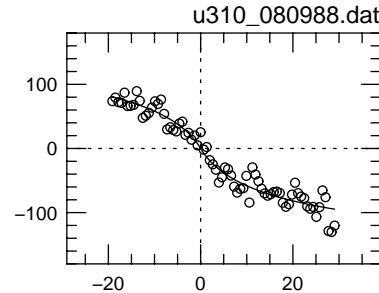
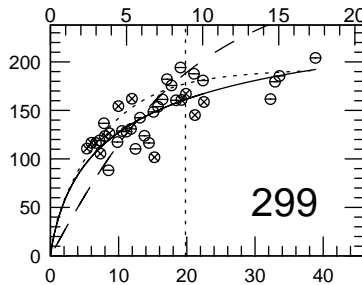
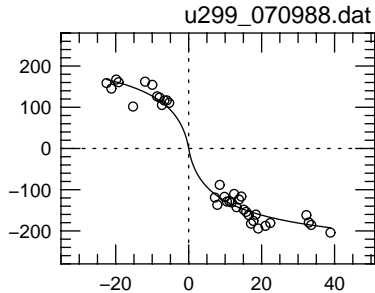
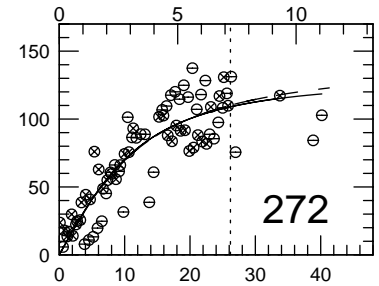
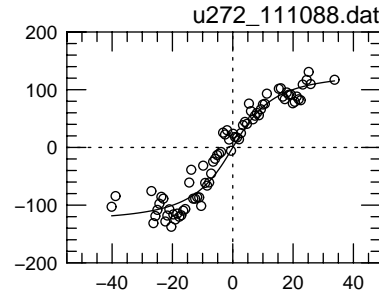
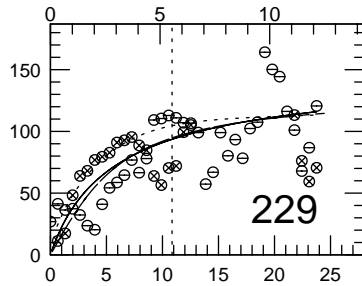
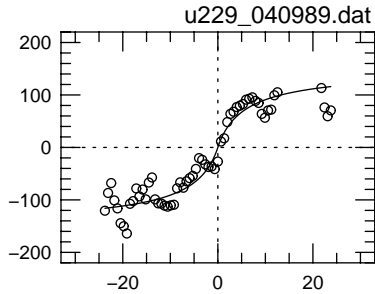


Distance from center [ " ↓ ; kpc ↑ ]

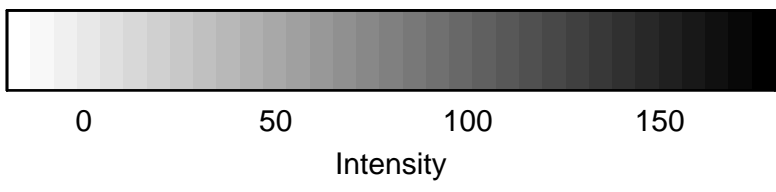
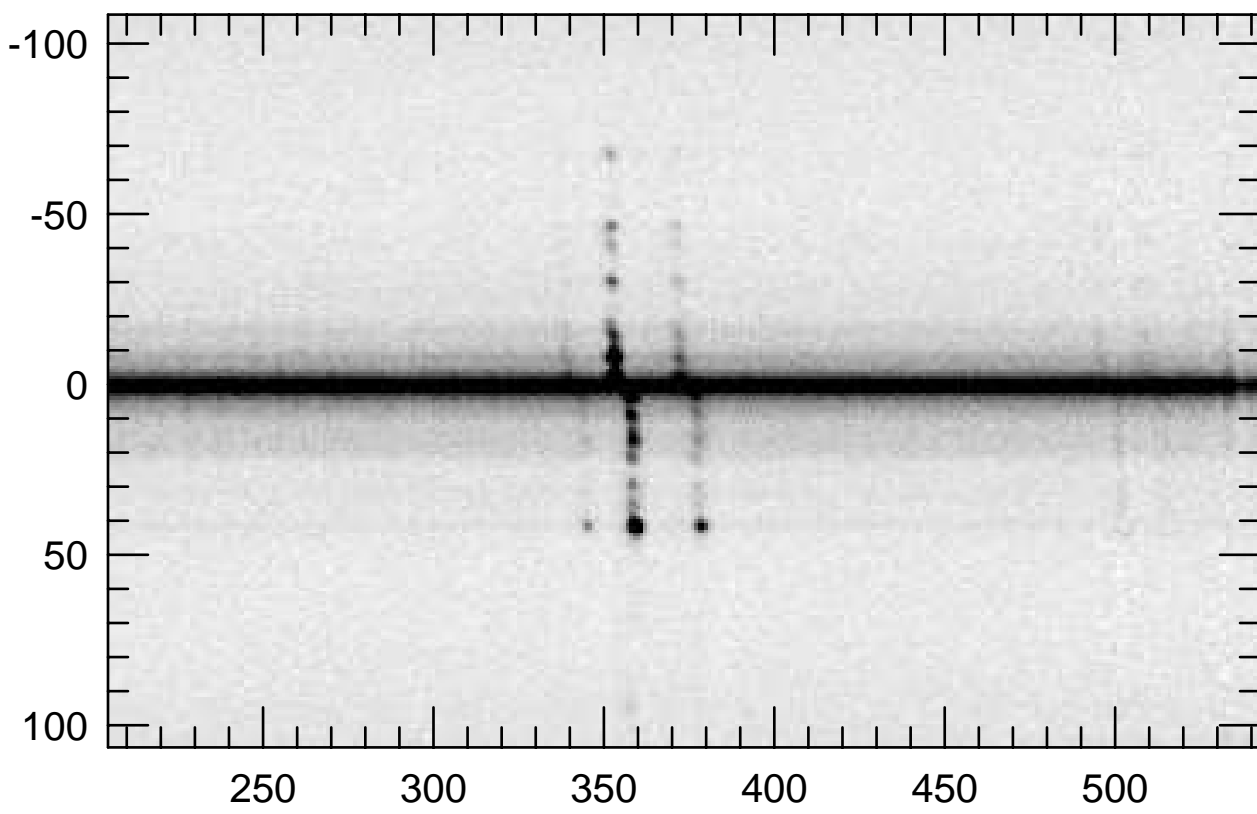




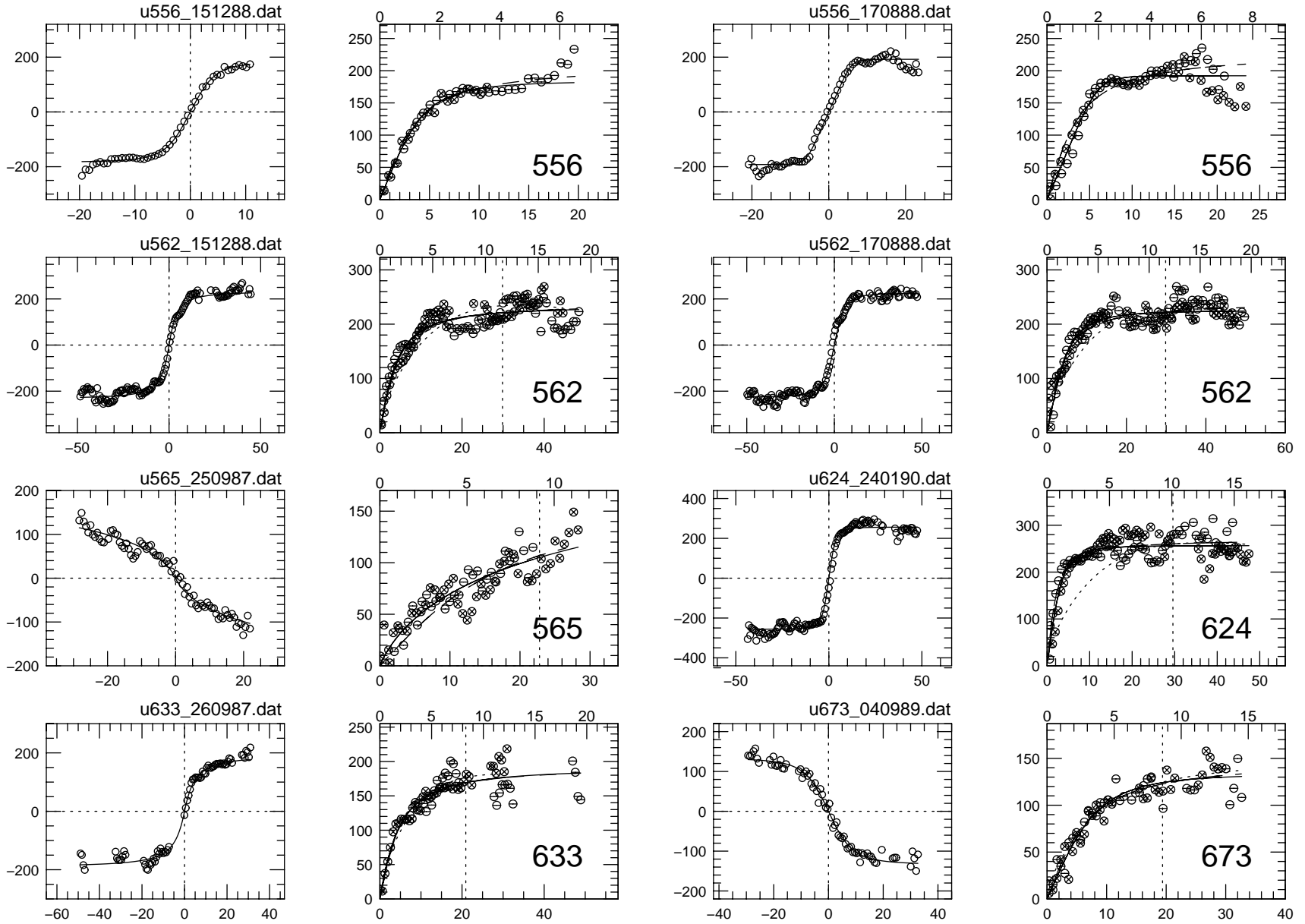
Line-of-Sight Velocity ( $\text{km s}^{-1}$ )



Distance from center [ "  $\downarrow$  ; kpc  $\uparrow$  ]



Line-of-Sight Velocity ( $\text{km s}^{-1}$ )



Distance from center [ "  $\downarrow$  ; kpc  $\uparrow$  ]

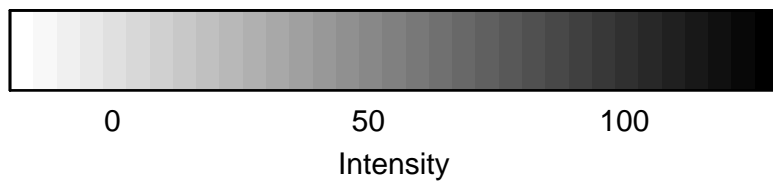
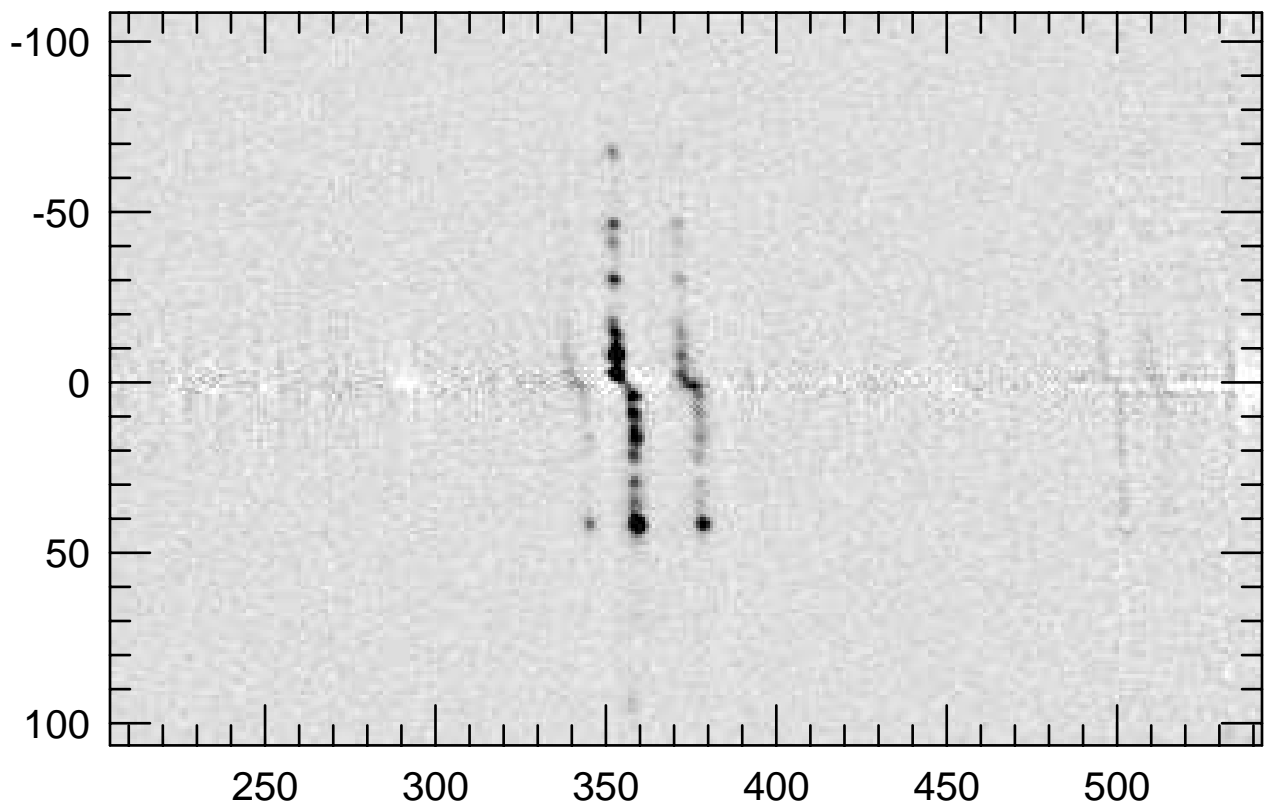


TABLE 3  
SPECTROSCOPY PARAMETERS

UGC	n	<i>i</i>	<i>cz</i> <sub>LG</sub>	<i>cz</i> <sub>CMB</sub>	<i>W</i> <sub>15</sub>	<i>W</i> <sub>20</sub>	<i>V</i> <sub>max</sub>	<i>V</i> <sub>2.2</sub>	<i>V</i> <sub>opt</sub>	<i>W</i> <sub>hist</sub>	<i>W</i> <sub>prob</sub>	<i>ls</i> <sub>m</sub>	<i>ls</i> <sub>r</sub>	<i>D</i>	<i>r</i> <sub>max</sub>	<i>r</i> <sub>kpc</sub>	<i>m</i> <sub>c</sub> <sup>r</sup>	<i>M</i> <sub>c</sub> <sup>r</sup>	Ft
(1)	(2)	(3)	(4)	(5)	(6)	(7)	(8)	(9)	(10)	(11)	(12)	(13)	(14)	(15)	(16)	(17)	(18)	(19)	(20)
14	1	52	7482	6913	408.7	408.2	406.0	402.6	404.9	415.0	455.5	0.03	0.03	106.89	56.79	29.43	13.38	-21.76	1
111	1	71	6527	5986	229.6	231.1	237.4	229.3	0.0	227.6	267.1	0.21	0.18	93.24	27.00	12.20	14.69	-20.16	2
166	1	58	5066	4507	277.1	278.7	289.4	287.6	289.3	277.7	337.5	0.22	0.28	72.37	42.26	14.83	14.04	-20.26	1
179	1	59	4679	4124	228.5	232.9	251.5	230.3	244.2	237.8	316.4	0.22	0.26	66.84	35.99	11.66	14.72	-19.40	1
195	2	76	5874	5356	248.4	247.2	261.5	242.4	258.7	252.4	299.8	0.25	0.29	83.92	32.38	13.17	14.16	-20.46	2
210	1	65	4681	4129	226.2	229.0	269.8	231.6	255.3	258.3	318.9	0.30	0.30	66.87	30.89	10.01	14.59	-19.53	2
229	1	52	7432	6879	246.2	247.4	286.5	231.3	261.4	249.0	320.5	0.35	0.24	106.17	23.76	12.23	15.01	-20.12	1
272	1	68	4027	3551	224.2	224.7	252.7	232.3	251.6	225.5	271.9	0.39	0.39	57.53	40.17	11.20	14.42	-19.38	1
299	1	58	6532	5986	383.9	379.1	442.2	370.6	413.9	393.1	418.6	0.33	0.33	93.32	38.87	17.59	14.32	-20.53	1
310	1	79	4884	4339	175.3	179.1	190.2	170.5	0.0	163.6	215.2	0.48	0.48	69.77	29.04	9.82	14.56	-19.66	2
346	2	66	6097	5556	281.3	279.7	303.0	280.3	0.0	277.5	323.6	0.40	0.40	87.10	22.17	9.36	14.25	-20.45	2
533	1	71	5642	5142	266.3	265.9	269.4	243.9	266.2	231.5	309.0	0.38	0.29	80.60	33.00	12.89	14.58	-19.96	2
540	1	53	5190	4670	246.9	246.1	263.0	216.4	260.2	233.8	283.1	0.58	0.52	74.15	18.44	6.63	13.62	-20.73	2
562	2	68	5669	5150	419.6	416.6	477.6	469.0	476.5	496.3	546.2	0.11	0.09	80.98	49.11	19.28	12.10	-22.44	1
565	1	75	5860	5342	215.9	218.6	233.6	213.2	0.0	199.4	261.4	0.51	0.53	83.71	28.31	11.49	14.30	-20.31	2
624	1	68	4985	4474	537.7	539.3	545.3	543.9	545.2	586.0	641.1	0.03	0.01	71.22	47.46	16.39	12.25	-22.01	1
633	1	80	5782	5271	327.1	328.5	365.3	337.3	353.6	357.7	408.5	0.18	0.19	82.60	48.91	19.59	13.61	-20.97	1
673	1	71	6460	5955	270.8	270.0	271.1	257.4	269.0	256.8	303.4	0.29	0.27	92.28	32.68	14.62	14.77	-20.05	1
732	2	54	5644	5145	282.3	281.9	366.2	319.8	382.1	315.0	370.1	0.38	0.24	80.63	37.08	14.49	13.70	-20.83	1
783	1	57	6138	5650	350.2	347.1	343.6	325.4	342.2	330.6	379.4	0.18	0.16	87.68	32.29	13.73	13.74	-20.98	2
784	1	59	5031	4626	323.3	326.0	308.5	306.1	308.4	316.0	348.1	0.05	-0.04	71.88	26.72	9.31	14.03	-20.26	1
810	1	79	5038	4546	221.4	222.1	275.6	238.0	271.7	237.0	344.3	0.40	0.44	71.97	45.11	15.74	13.85	-20.43	2
890	1	75	5045	4636	281.9	282.0	351.1	290.1	323.8	311.3	367.4	0.34	0.35	72.07	61.92	21.64	13.30	-20.99	2
899	1	58	9384	8912	337.4	333.9	405.9	348.7	384.1	371.8	429.3	0.27	0.30	134.06	25.58	16.63	14.48	-21.15	2
927	1	58	6206	5723	274.0	270.6	314.0	301.4	0.0	273.5	346.5	0.32	0.33	88.65	32.60	14.01	13.42	-21.32	2
987	1	77	4853	4374	351.6	352.5	374.2	368.5	363.9	389.1	426.1	-0.01	-0.09	69.33	57.92	19.47	12.81	-21.40	1
1037	1	69	15692	15221	492.8	500.1	499.9	491.8	499.3	513.7	553.6	0.14	0.13	224.17	24.73	26.88	14.18	-22.57	2
1053	1	49	9121	8718	440.6	442.0	469.9	459.8	0.0	462.5	501.3	0.13	0.18	130.30	19.69	12.44	13.64	-21.94	2
1083	1	62	4657	4216	348.8	347.8	306.3	300.3	295.5	327.1	371.4	-0.03	-0.08	66.52	33.86	10.92	13.76	-20.36	1
1094	1	77	4546	4076	421.3	418.7	486.1	441.4	480.0	461.4	499.6	0.30	0.29	64.94	45.42	14.30	12.75	-21.32	2
1118	1	78	3612	3214	220.1	217.4	229.6	218.5	0.0	212.4	266.5	0.44	0.59	51.59	55.77	13.95	13.56	-20.01	2
1152	2	58	6805	6342	302.3	299.7	312.8	309.6	311.2	318.5	357.9	0.12	0.09	97.21	29.02	13.68	14.36	-20.58	2
1174	1	52	17072	16708	457.3	458.0	472.6	465.5	471.6	497.2	544.5	0.29	0.27	243.89	24.58	29.06	14.42	-22.51	2
1192	1	55	3110	2693	317.2	318.6	308.0	305.6	0.0	305.3	354.6	0.08	0.06	44.43	61.23	13.19	12.37	-20.87	1

# Figure 4 – Maximal Extent of ORCs

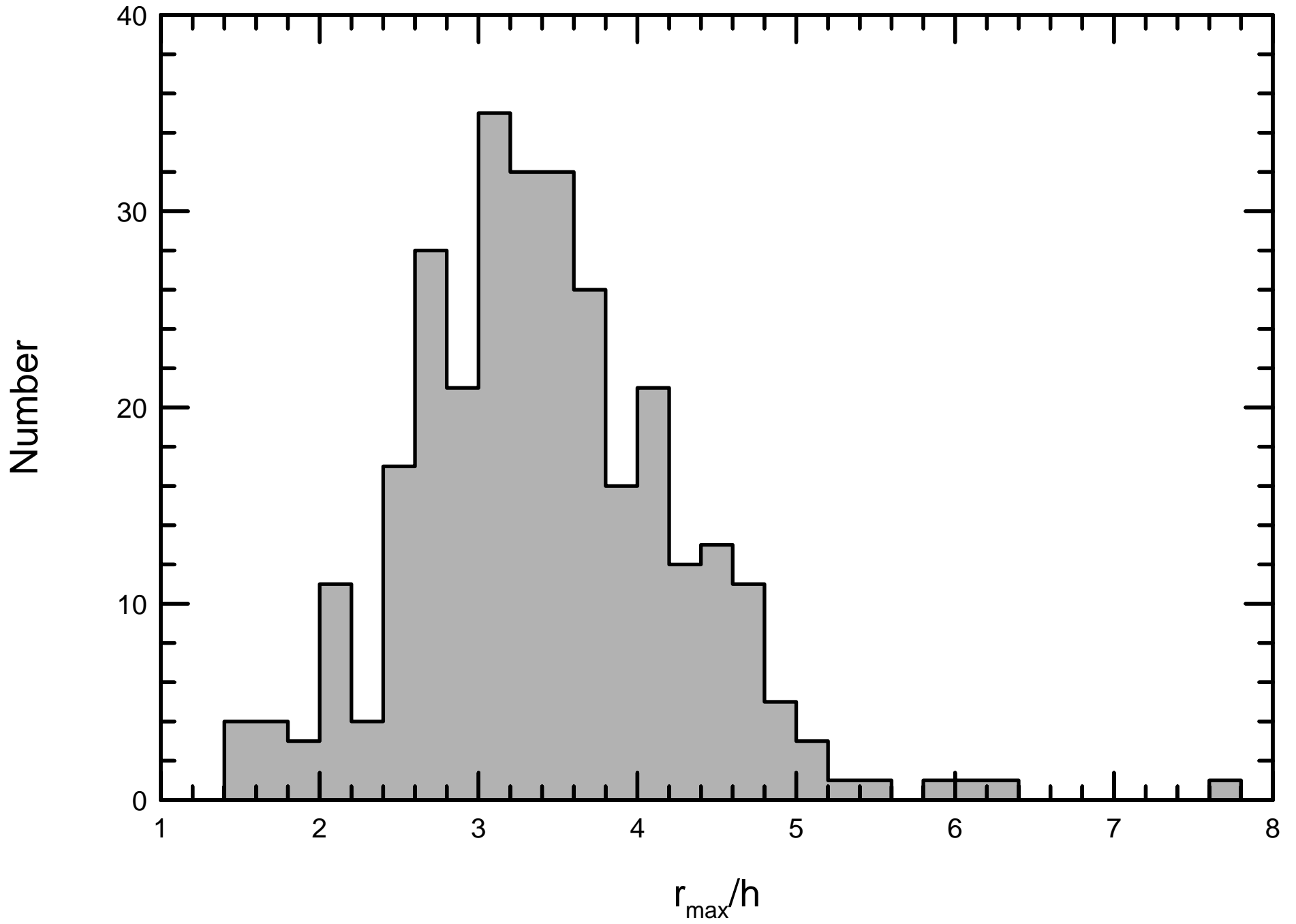


Figure 5 – Courteau vs Rubin

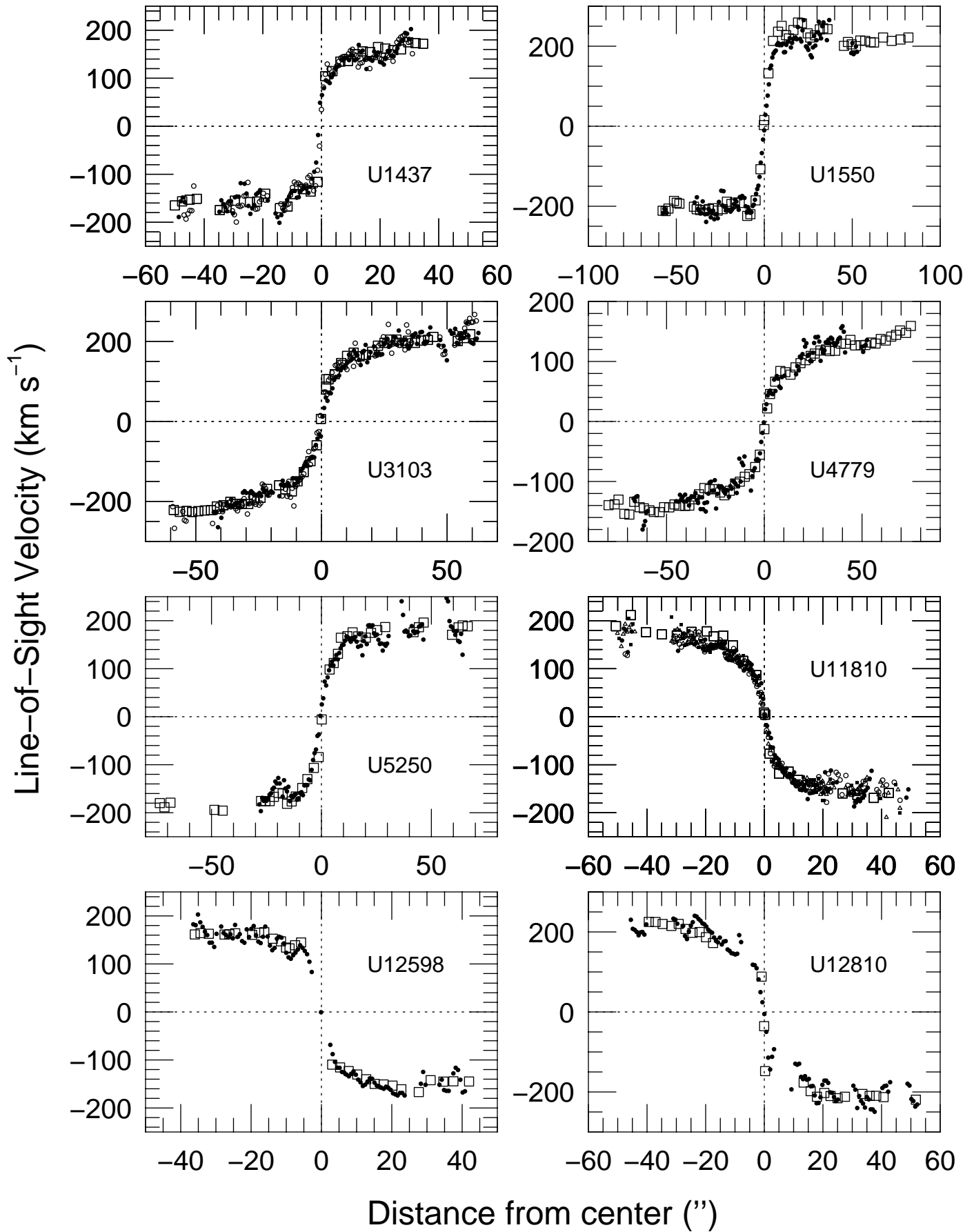




Figure 6 – Courteau vs Mathewson

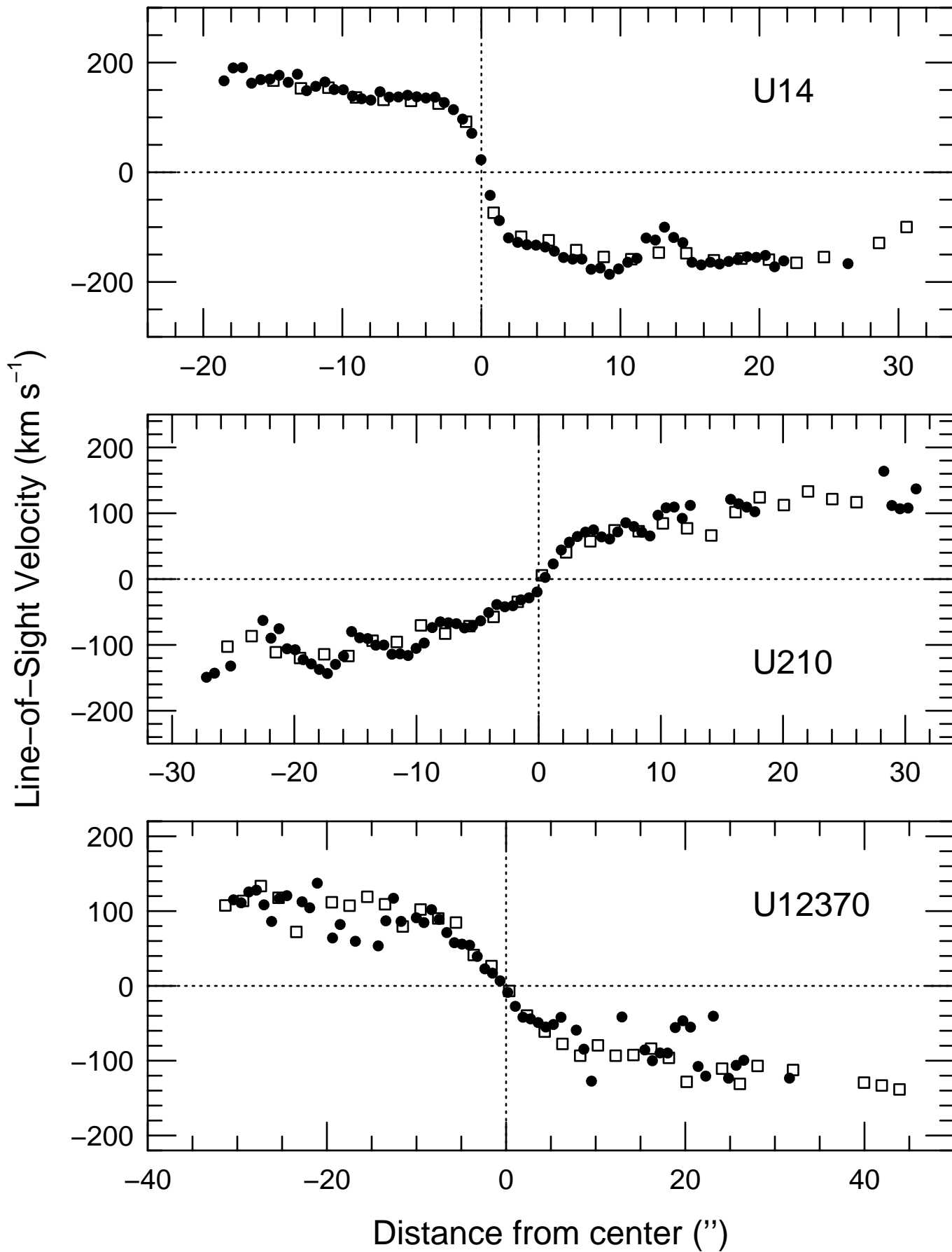


TABLE 6  
FIT PARAMETERS FOR CF GALAXIES

Galaxy	Multi-Parameter Fits					Arctan Fits		
	$v_c$	$r_c$	$\gamma$	$\beta$	$\chi^2_\nu$	$v_c$	$r_c$	$\chi^2_\nu$
u14 080988	-164.8	1.6	1.4	0.0	5.5	-166.7	1.1	5.2
u111 060988	122.8	4.5	1.3	0.0	1.8	127.0	3.9	2.4
u166 020989	124.0	12.2	4.7	0.0	2.9	161.0	7.7	3.1
u179 020989	-112.8	7.8	1.9	0.0	4.6	-125.9	5.2	4.8
u183 111088	234.2	12.8	10.2	0.0	1.8	235.7	0.7	2.4
u195 020989	-139.6	3.9	1.1	0.0	4.3	-134.8	3.3	4.3
u195 261089	-182.9	4.8	0.7	0.0	5.0	-132.5	4.5	5.3
u210 040989	148.9	6.1	1.0	0.0	5.7	146.2	6.2	6.3
u229 040989	150.1	5.4	0.9	0.0	10.9	132.2	5.2	10.6
u272 111088	128.9	14.6	1.8	0.0	6.2	147.1	10.9	7.0
u299 070988	-292.7	4.9	0.6	0.0	3.3	-350.8	17.6	49.8
u310 080988	-173.2	13.5	0.7	0.0	3.5	-114.1	9.5	3.6
u346 180888	-214.8	8.3	0.9	0.0	2.5	-170.1	6.1	2.4
u346 241289	-249.5	5.6	0.6	0.0	4.5	-155.4	5.6	4.8
u533 060988	142.6	11.5	1.6	0.0	4.9	151.4	7.9	5.0
u540 240190	-154.5	13.2	1.3	0.0	2.8	-140.8	7.8	2.9
u556 151288	184.0	4.8	2.4	0.0	1.5	211.3	3.0	2.0
u556 170888	192.1	6.1	5.9	0.0	5.4	229.6	3.1	9.3
u562 151288	233.1	4.8	1.4	0.0	6.1	239.9	3.7	7.9
u562 170888	225.4	6.1	2.1	0.0	9.3	241.5	3.5	9.8
u565 250987	-272.5	14.8	0.6	0.0	1.6	-168.0	14.6	2.6
u624 240190	256.7	3.8	2.3	0.0	10.4	270.5	1.8	8.2
u633 260987	191.2	5.4	1.3	0.0	2.7	193.5	4.2	2.7
u673 040989	-133.9	9.3	2.3	0.0	1.5	-149.8	5.7	1.6
u679 260987	-102.0	16.3	2.5	0.0	4.3	-125.5	12.3	4.4
u732 260987	-406.2	5.1	0.4	0.0	1.7	-161.8	5.7	1.9
u732 271089	-159.4	10.9	1.3	0.0	1.9	-159.6	7.8	1.9
u783 190888	169.7	2.3	0.8	0.0	3.7	152.8	3.0	4.3
u784 030989	134.6	2.8	2.0	0.0	2.8	142.2	1.5	2.5
u810 260987	285.3	8.8	0.5	0.0	5.8	145.0	6.0	9.0
u890 180888	238.8	8.9	0.7	0.0	4.6	161.8	6.7	6.5
u899 080988	-321.9	0.9	0.4	0.0	4.1	-164.8	2.2	4.6
u927 260987	208.2	4.3	0.6	0.0	3.0	137.7	4.7	3.6
u987 240190	174.2	7.2	3.6	0.2	6.5	216.4	3.3	8.5
u1037 020989	-249.2	3.2	1.8	0.0	2.9	-264.0	1.9	2.7
u1053 261089	200.2	0.8	0.8	0.0	7.8	177.6	0.8	3.3
u1083 060988	-126.7	5.9	4.7	0.2	5.6	-147.8	1.9	7.2
u1094 260987	-296.3	7.9	0.9	0.0	4.2	-267.9	8.5	4.7
u1118 070988	-142.9	21.4	1.2	0.0	2.6	-131.2	14.8	2.7
u1152 111088	-115.2	8.4	2.7	0.5	3.3	-147.4	2.5	3.3
u1152 190888	-122.8	9.1	2.2	0.5	2.5	-151.4	2.6	2.4
u1174 020989	196.6	6.4	4.4	0.0	8.3	228.3	3.6	9.5
u1192 180888	129.3	5.4	1.5	0.0	3.8	134.4	3.8	3.7
u1235 030989	182.9	2.6	0.5	0.0	5.2	103.8	2.9	5.8
u1426 040989	-217.6	11.3	0.8	0.0	3.5	-161.4	8.5	3.7
u1437 250987	158.2	8.9	1.3	0.6	8.6	166.3	2.0	8.0
u1437 251289	118.0	25.3	2.5	0.9	7.7	160.5	1.2	8.7

Figure 7a – Courteau vs Vogt

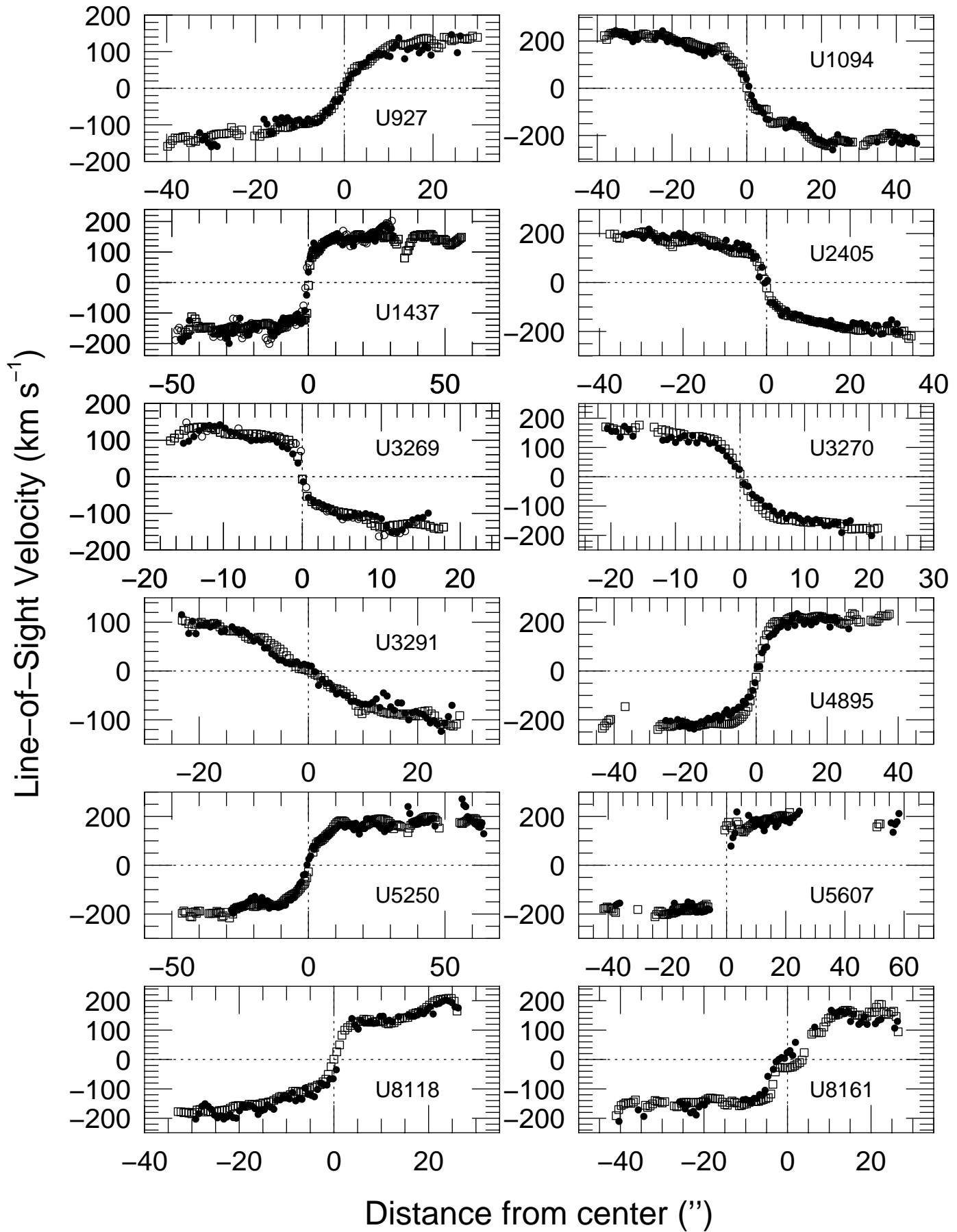


Figure 7b – Courteau vs Vogt

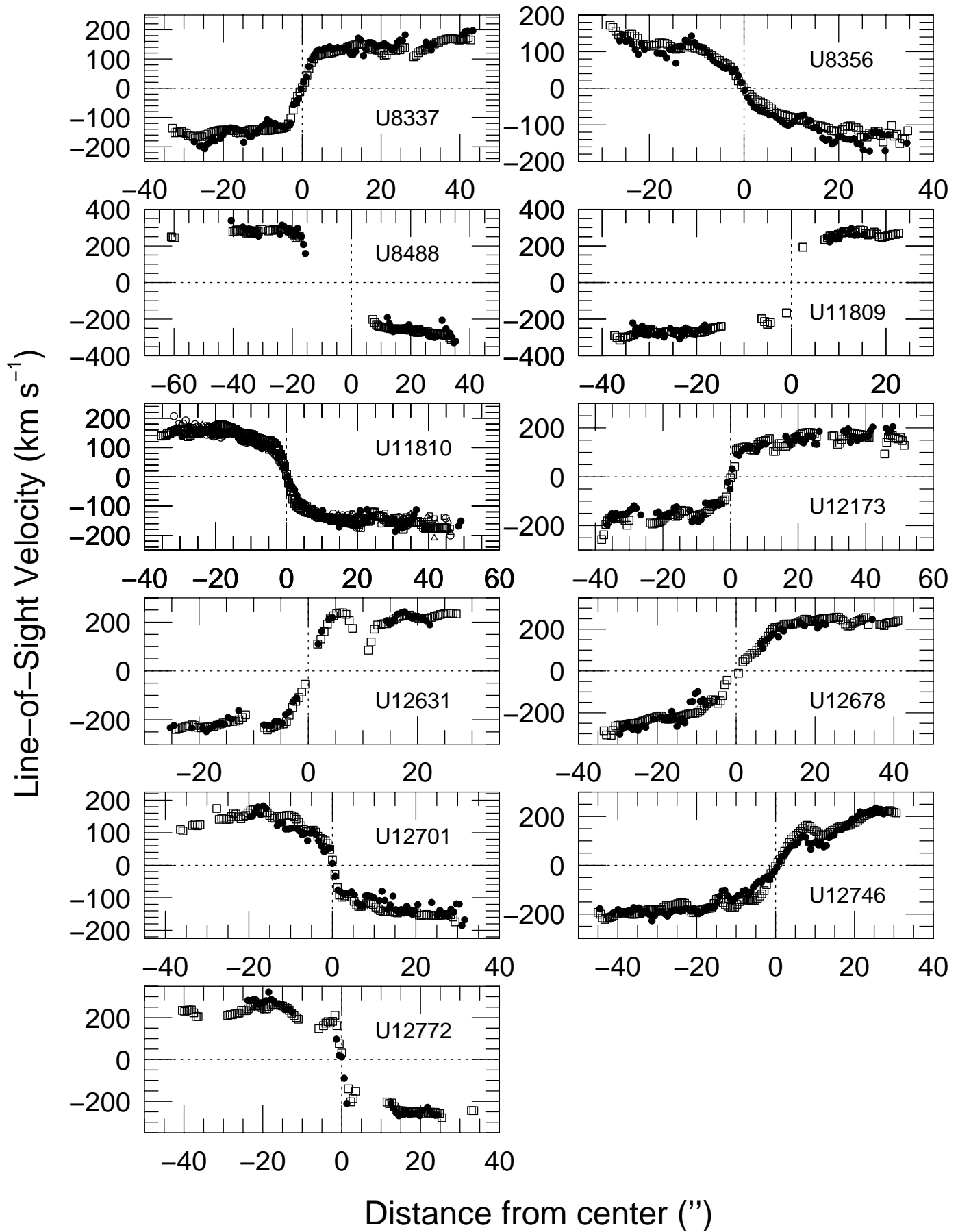


TABLE 7  
FIT PARAMETERS FOR MAT GALAXIES

Galaxy	Multi-Parameter Fits							Arctan Fits			
	$v_0$	$r_0$	$v_c$	$r_c$	$\gamma$	$\beta$	$\chi^2_\nu$	$v_c$	$r_c$	$\chi^2_\nu$	$\Delta cz$
1-g6.orc	2251.3	-2.01	-268.3	21.8	0.7	0.0	7.4	-181.5	16.6	7.5	6.3
1-g7.orc	5001.5	0.69	0.1	1019.0	-0.1	0.0	5.7	135.9	5.4	4.4	7.5
10-g4.orc	2439.7	-5.28	-179.9	23.1	0.8	0.0	5.4	-142.4	22.5	5.2	13.7
101-g20.orc	5839.9	0.12	-186.0	3.7	1.1	0.0	42.5	-156.4	0.6	17.6	-5.1
101-g5.orc	6641.6	0.29	212.1	13.7	1.4	0.0	5.1	212.9	9.6	4.6	3.6
102-g10.orc	4702.9	-0.64	172.9	5.3	1.5	0.0	8.1	178.1	3.6	8.1	4.9
102-g15.orc	5017.8	-0.07	-116.2	2.1	4.2	0.0	6.2	-120.7	0.8	7.0	-0.2
102-g7.orc	5015.6	-1.88	-183.3	5.1	1.6	0.0	4.0	-189.5	3.0	3.9	1.6
103-g13.orc	4661.4	-1.71	213.4	10.1	2.1	0.0	8.6	229.2	5.8	8.9	-2.6
103-g15.orc	4586.3	-2.26	131.8	12.5	2.4	0.0	2.7	151.5	7.9	2.9	3.3
103-g39.orc	4483.6	-0.30	-119.3	4.6	0.7	0.0	7.3	-94.0	4.7	7.4	0.6
104-g52.orc	3881.1	1.68	131.8	17.5	1.9	0.0	5.6	145.6	11.4	5.6	-0.9
105-g20.orc	5668.1	-2.10	151.1	17.0	1.6	0.0	7.6	170.6	13.5	7.1	-3.9
105-g3.orc	4863.6	-1.03	-195.0	8.0	1.1	0.0	6.8	-184.6	6.4	6.6	3.6
106-g12.orc	4151.9	-0.18	121.0	4.5	2.0	0.0	2.1	131.0	2.8	2.2	-3.1
106-g8.orc	3226.7	0.25	179.6	10.6	1.7	0.0	6.1	196.2	7.7	6.0	-1.3
107-g24.orc	5110.1	0.71	154.5	12.1	2.2	0.0	1.0	174.0	7.7	1.3	1.1
107-g36.orc	3102.2	-3.91	-186.7	2.0	0.9	0.0	7.0	-183.3	3.3	5.3	6.2
108-g11.orc	2985.0	-0.29	-202.4	20.8	2.3	0.0	16.3	-236.7	15.2	17.2	6.0
108-g13.orc	2934.8	-1.21	215.8	13.4	0.8	0.0	2.8	152.8	9.6	3.5	-0.2
108-g19.orc	2952.0	0.50	130.0	2.0	10.0	0.3	10.3	135.2	0.0	10.2	-4.0
108-g6.orc	5290.2	-4.61	501.3	31.6	0.9	0.0	10.2	320.2	16.1	9.9	-46.8
109-g32.orc	3353.5	3.80	-513.0	9.7	0.3	0.0	14.5	-140.7	19.6	13.3	-8.5
111-g9.orc	4206.7	2.35	-154.8	8.6	1.3	0.0	6.3	-159.0	6.9	6.0	-10.3
112-g10.orc	5993.6	3.40	168.9	8.1	1.1	0.0	6.9	154.3	5.8	6.4	19.6
113-g21.orc	4823.6	-0.32	-93.6	13.8	4.7	0.0	6.2	-111.7	7.3	6.7	1.6
113-g6.orc	8434.5	-1.02	170.7	7.5	1.5	0.0	44.5	180.4	5.7	43.5	5.5
114-g21.orc	6377.7	0.95	-146.5	4.6	1.5	0.0	6.2	-151.3	3.3	5.8	-0.3
116-g12.orc	1152.2	-4.46	-147.6	28.7	0.8	0.0	3.4	-118.1	24.9	3.4	-0.8
116-g14.orc	5425.2	-2.62	-177.9	10.8	1.2	0.0	5.6	-176.6	8.6	5.2	8.2
117-g18.orc	5801.1	-1.17	-252.9	5.0	0.7	0.0	6.5	-202.9	6.1	8.4	6.1
117-g19.orc	5386.6	-0.04	-184.7	14.7	3.2	0.0	7.5	-211.4	8.3	8.4	0.6
120-g16.orc	3663.6	-8.40	214.7	12.4	1.0	0.0	3.8	192.9	10.4	4.0	-10.4
121-g26.orc	2217.3	2.12	151.2	5.1	1.5	0.0	6.3	153.8	3.2	5.9	-2.7
121-g6.orc	1228.9	-0.50	192.3	4.5	0.5	0.0	6.2	133.9	10.7	7.6	0.9
123-g15.orc	3217.6	-0.24	-169.2	3.7	0.9	0.0	6.1	-157.2	3.3	6.7	2.6
123-g16.orc	3196.6	-0.02	-145.0	8.0	0.9	0.0	5.4	-143.6	11.1	3.5	2.6
123-g23.orc	2915.9	-2.01	-214.2	22.0	1.1	0.0	2.7	-192.8	15.9	2.6	5.9
123-g9.orc	3210.6	-0.08	-178.8	5.6	0.8	0.0	10.3	-153.0	6.4	10.0	8.6
124-g15.orc	2625.8	-6.16	-223.8	37.1	1.1	0.0	3.0	-192.0	23.9	2.9	19.8
13-g16.orc	1772.5	5.08	148.4	52.3	1.1	0.0	5.1	122.2	32.7	5.0	16.5
13-g18.orc	4316.1	3.41	217.0	52.1	1.1	0.0	2.0	171.3	29.9	1.9	7.1
140-g1.orc	4332.1	-1.80	365.6	30.8	0.6	0.0	28.1	247.4	30.1	27.9	20.1
140-g24.orc	3178.0	-1.56	205.0	13.4	2.6	0.0	13.1	218.3	6.4	17.6	-5.0
140-g25.orc	2048.3	2.42	116.2	20.2	1.2	0.0	3.9	116.8	16.4	3.4	1.3
140-g28.orc	4873.2	-1.44	-8174.9	14.9	0.1	0.4	6.3	-98.1	4.6	8.1	-1.8
140-g33.orc	4674.7	0.27	-181.3	5.8	10.0	0.0	6.1	-212.5	2.6	15.3	-5.3

### Figure 8 – Courteau vs Amram

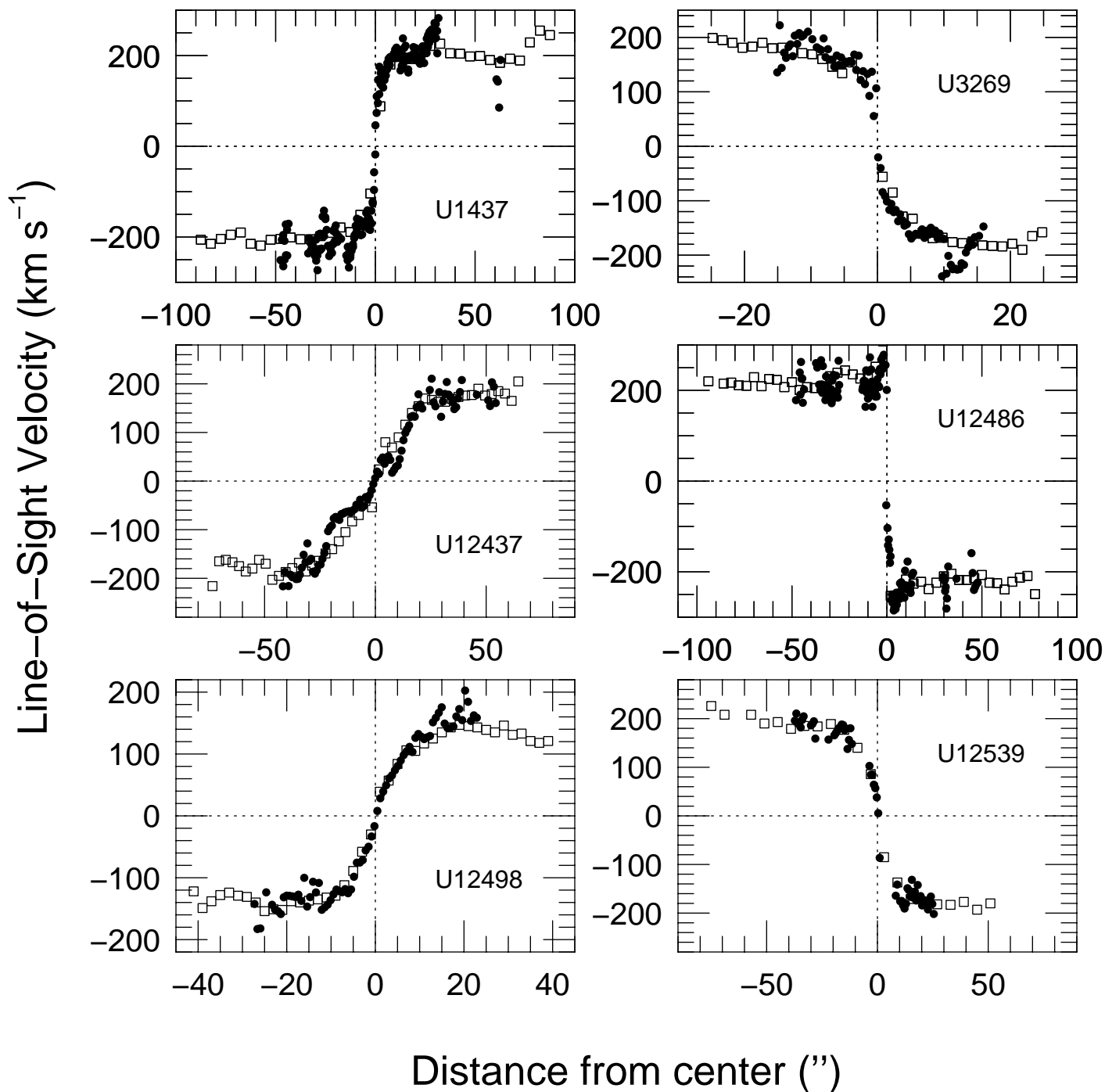


Fig. 9 – Arctan Models

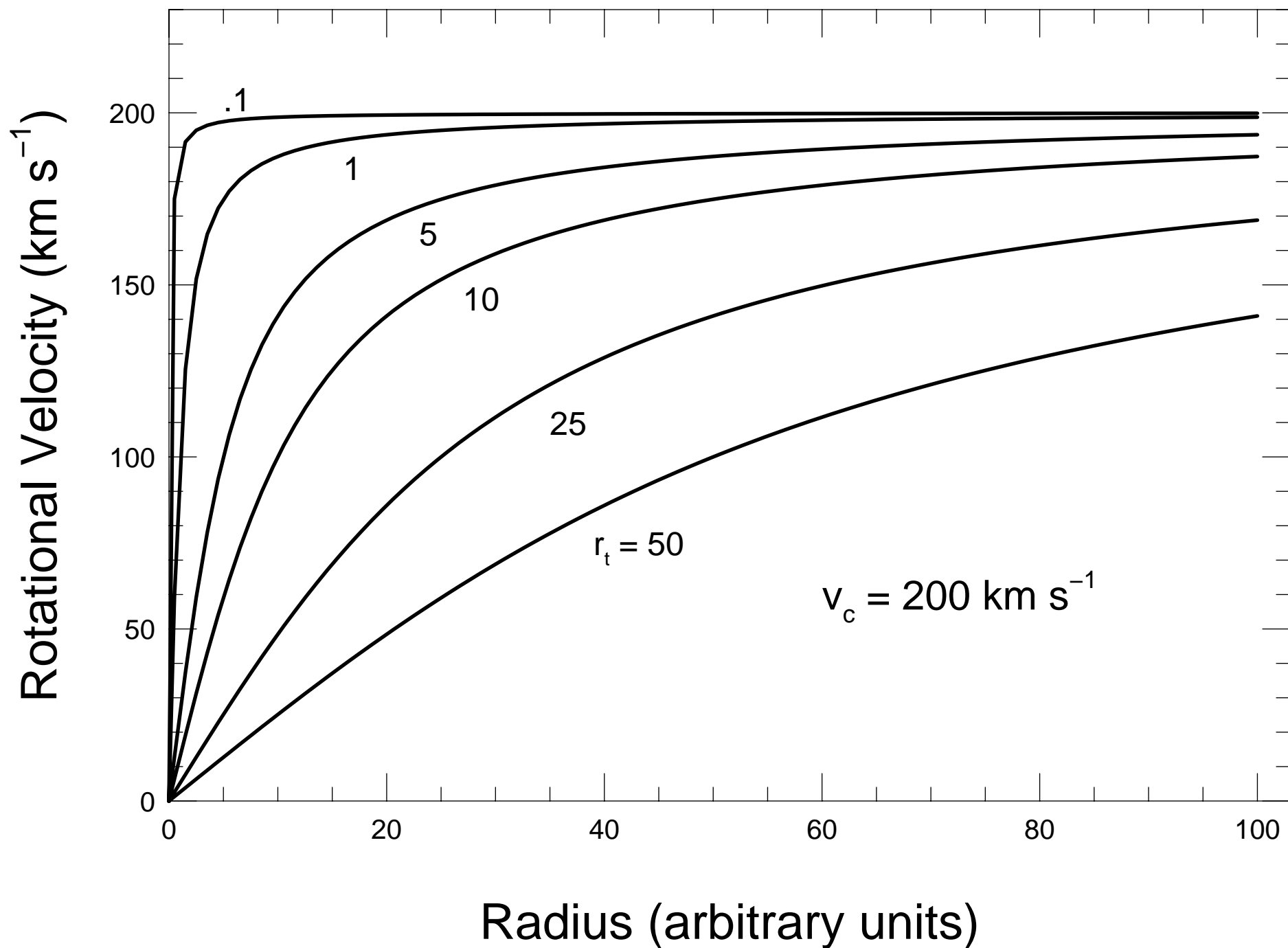


Figure 10 – Parametric Models /profiles/rcprofiles/simulrc.mgo

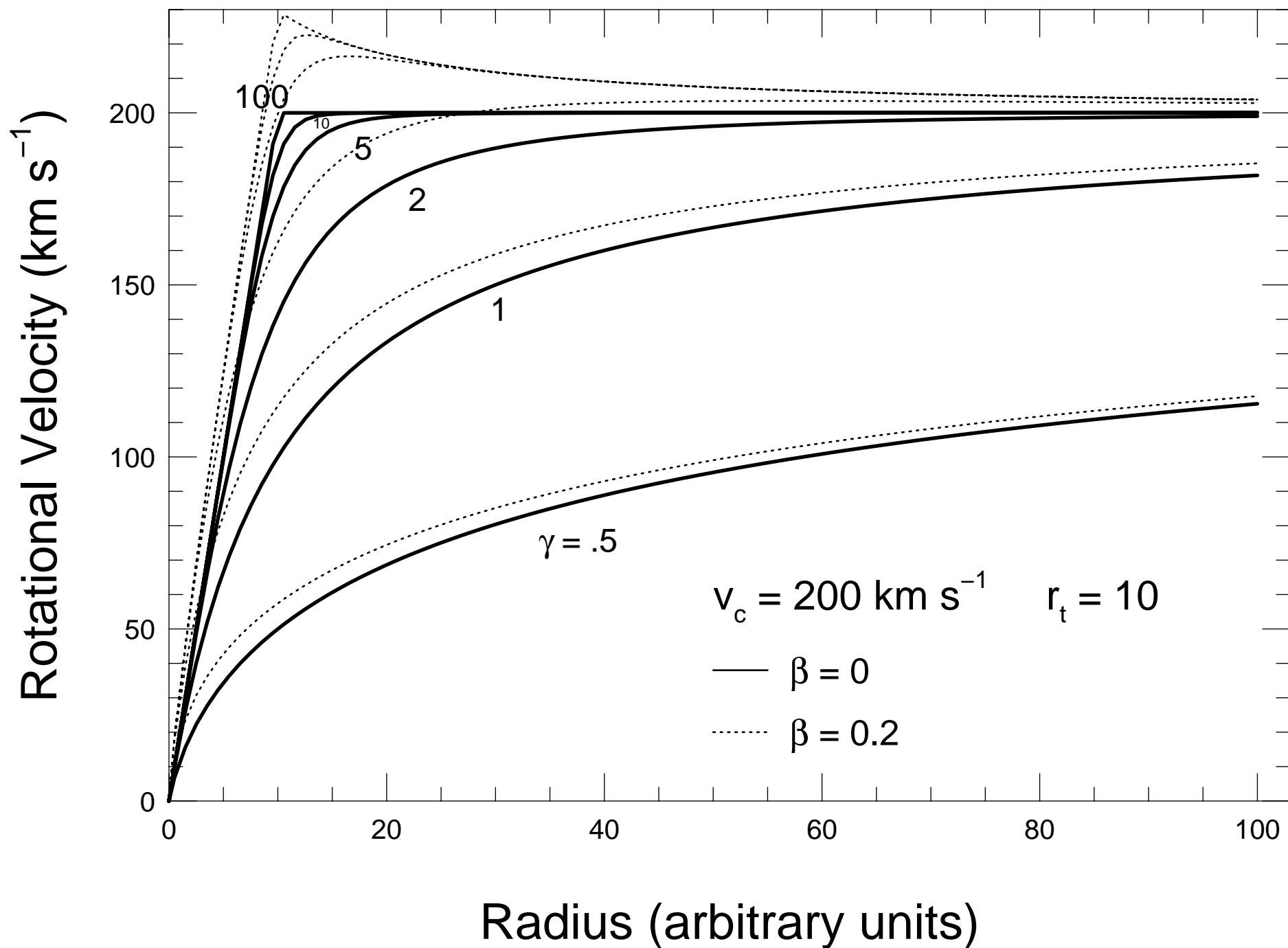




Figure 11

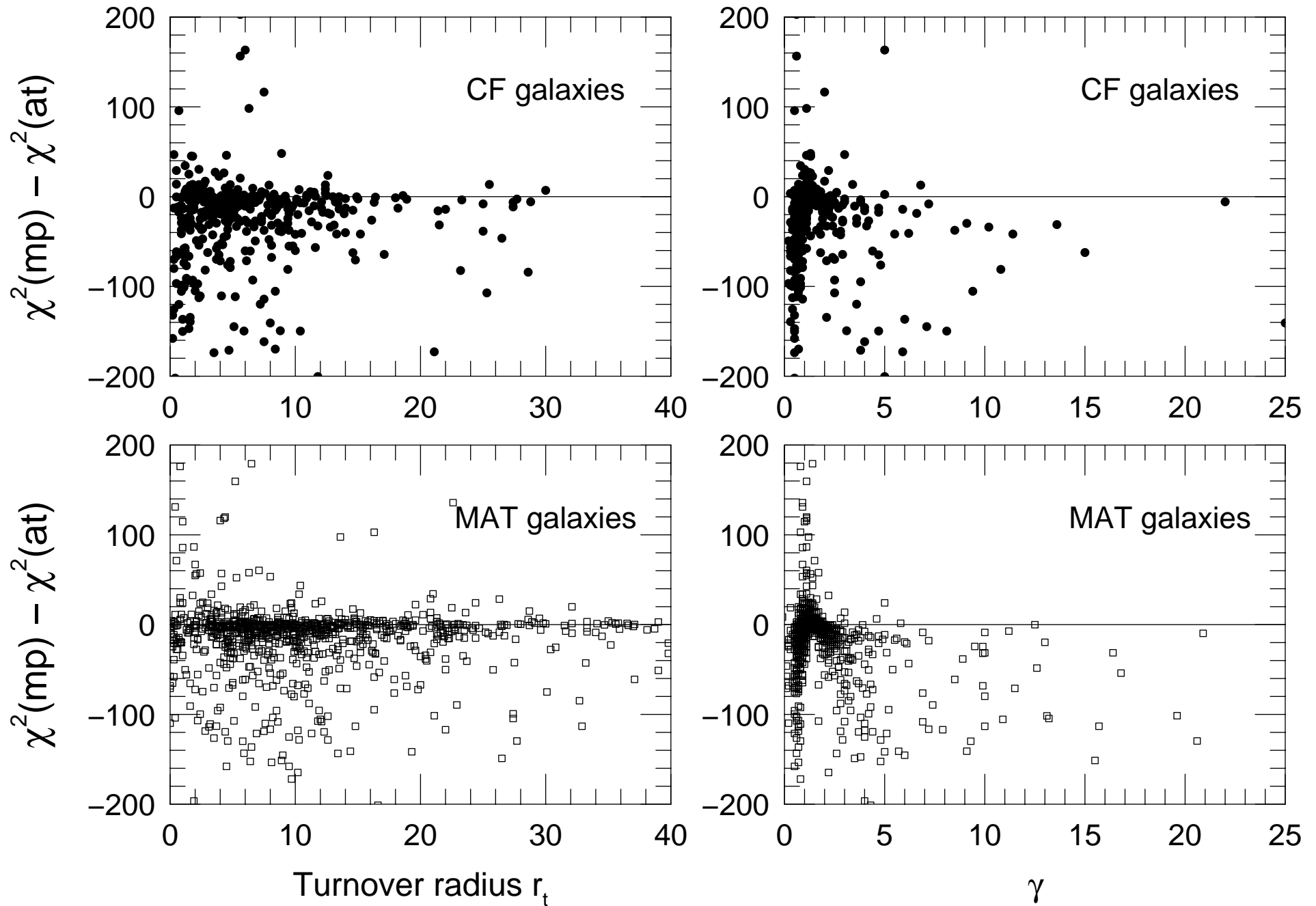
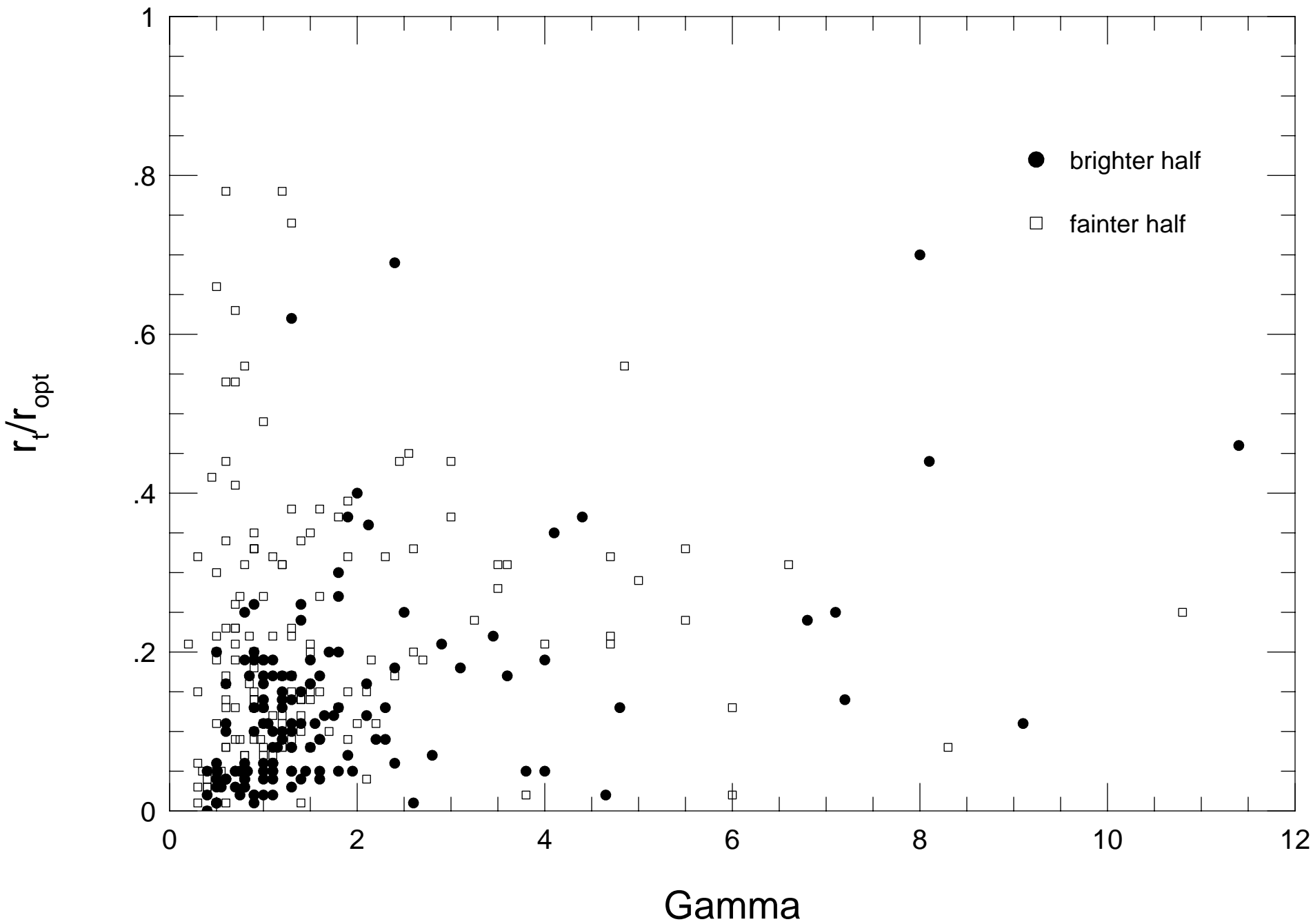


Figure 12



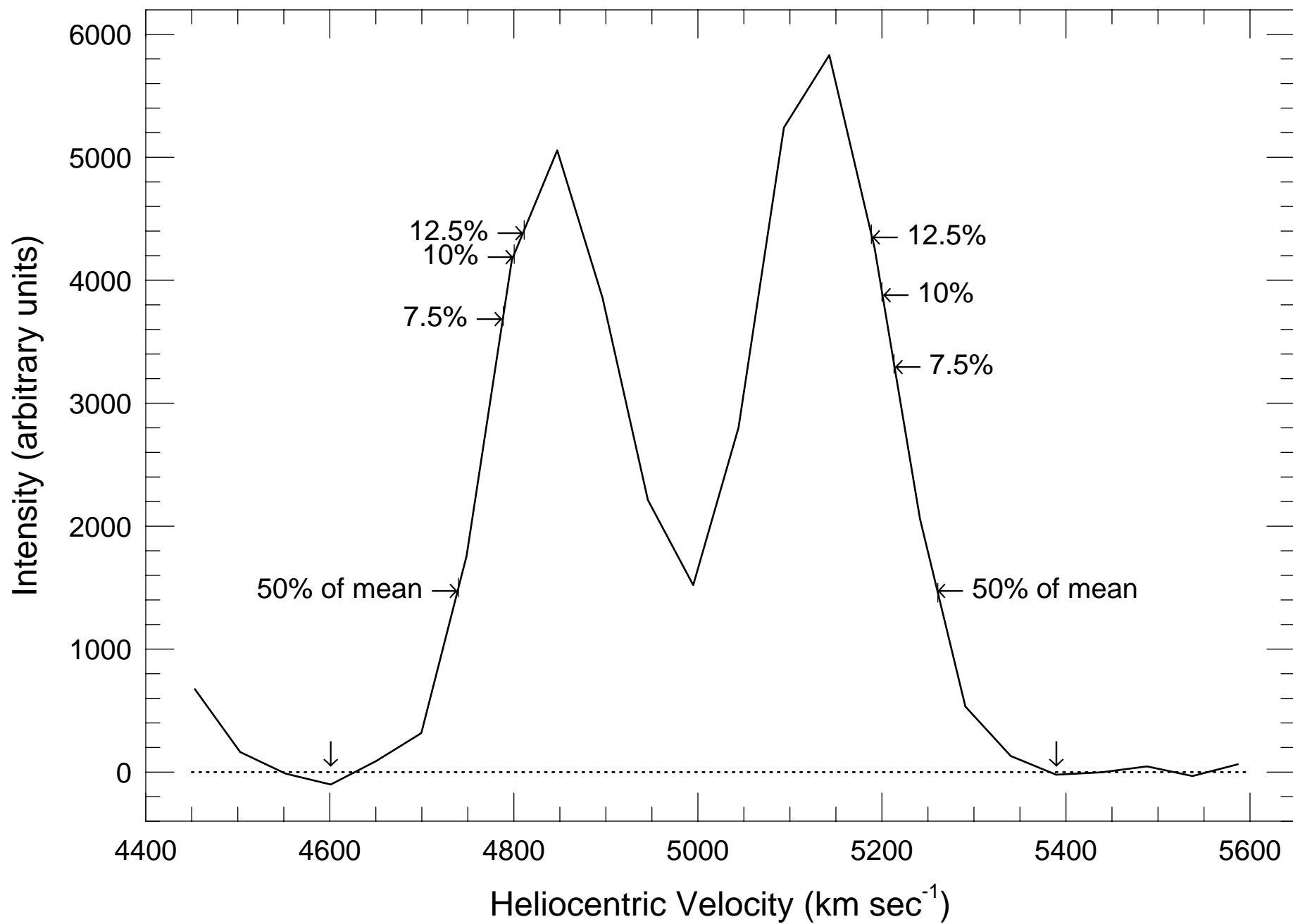


Figure 14

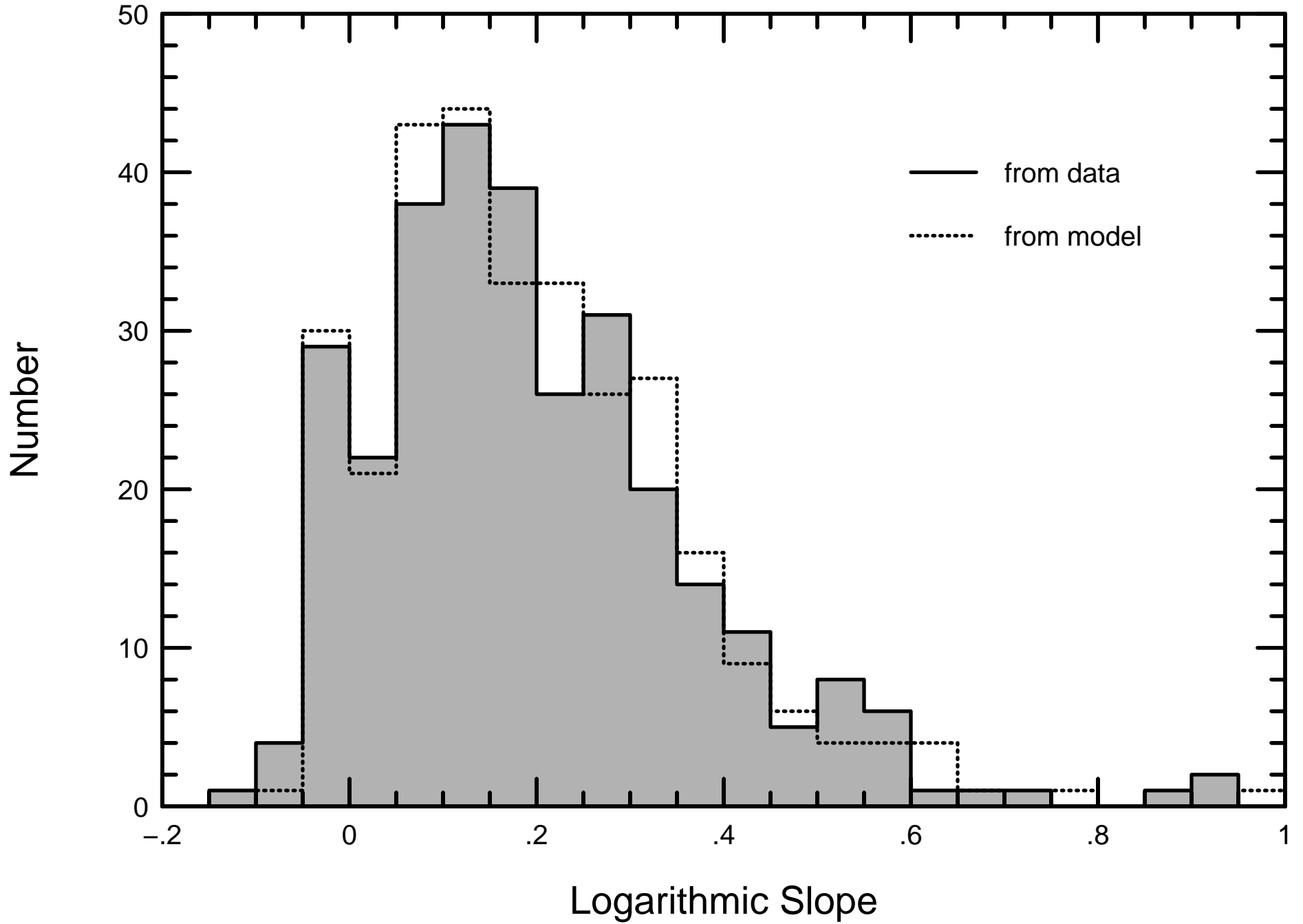


Figure 15

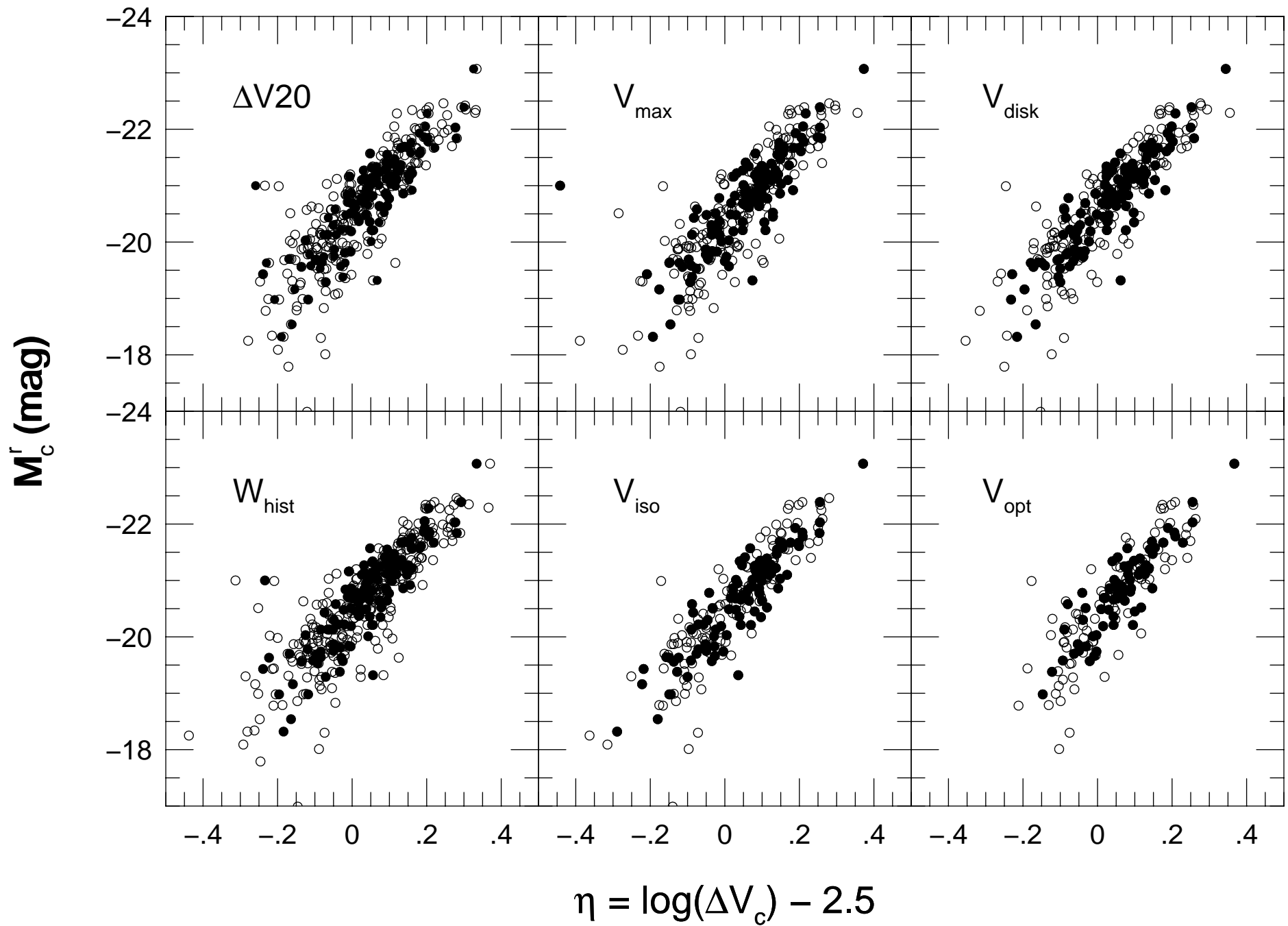


Figure 16

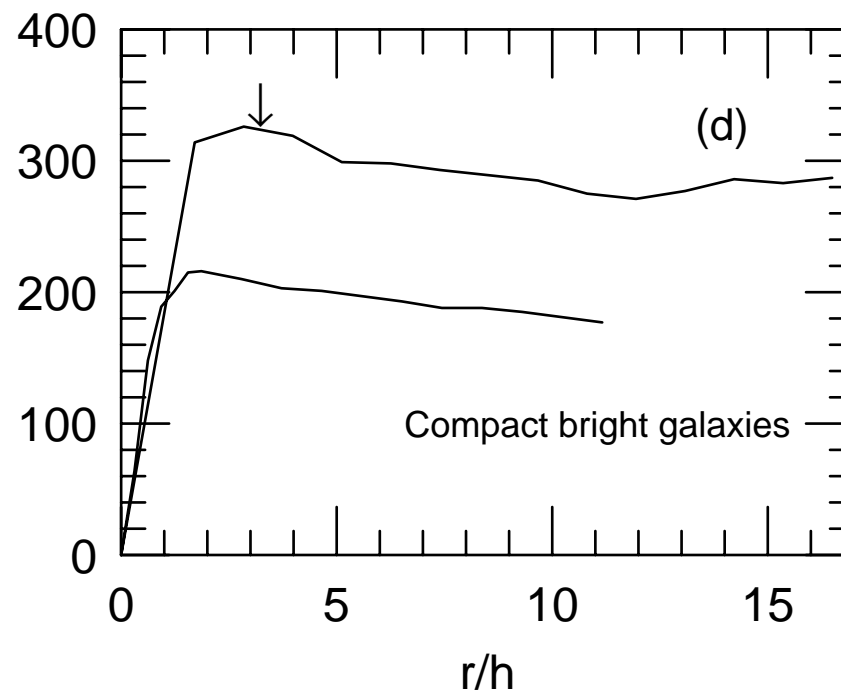
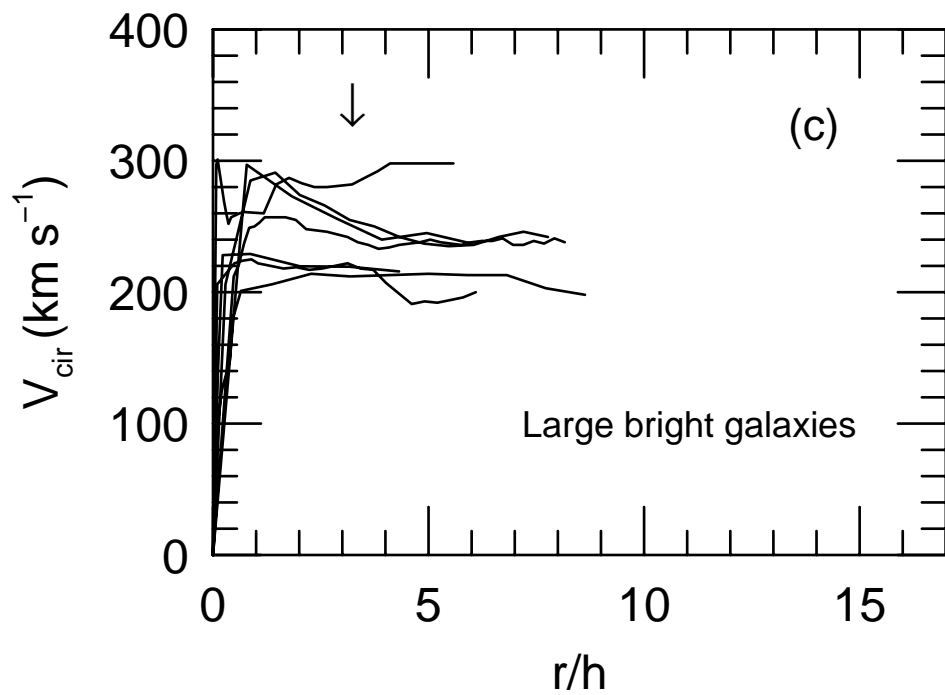
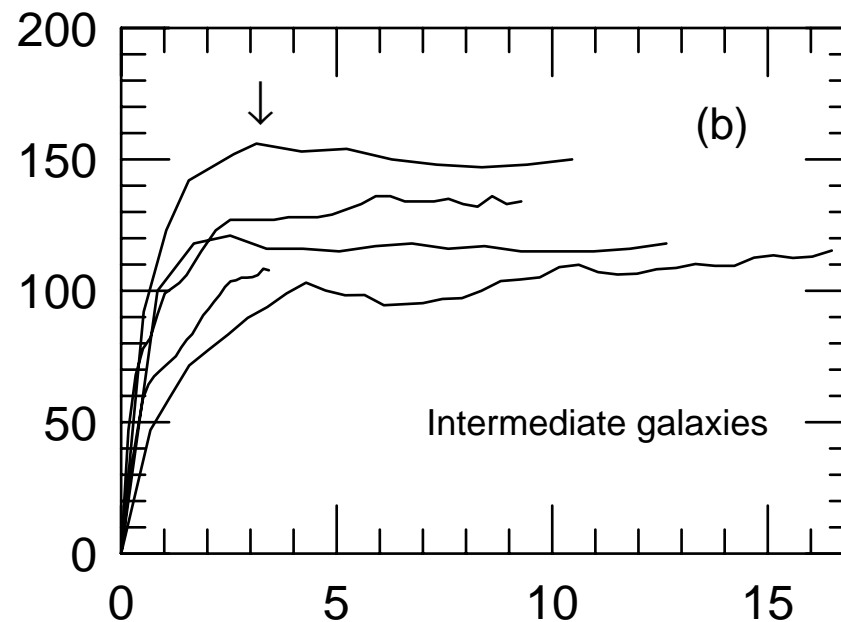
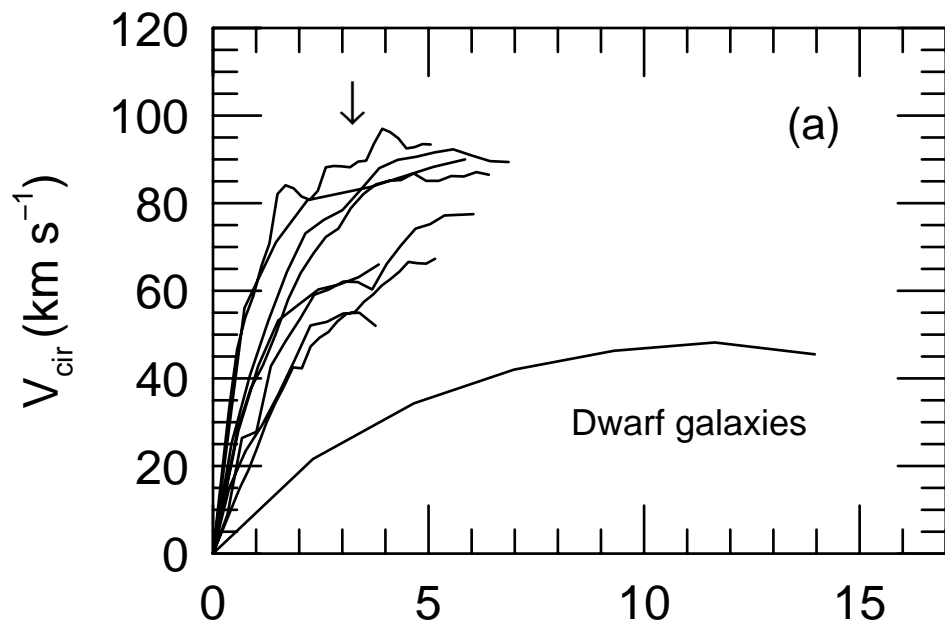


Figure 17

